Cell Reports

Article

Allocentric representation in the human amygdala and ventral visual stream

Graphical Abstract

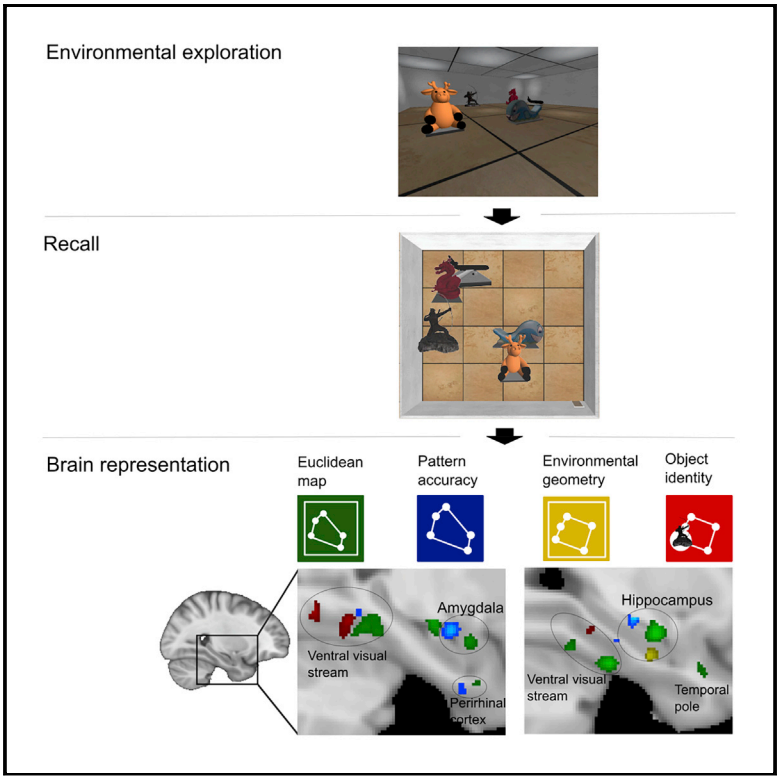

Authors

Hallvard Røe Evensmoen, Lars M. Rimol, Anderson M. Winkler, Richard Betzel, Tor Ivar Hansen, Hamed Nili, Asta Håberg

Correspondence

hjernemannen@gmail.com

In Brief

Evensmoen et al. demonstrate that the human brain encodes scaled and true Euclidean representations of allocentric space within an extensively connected medial temporal lobe network with no main connector hub. The network includes the parahippocampal cortex, fusiform cortex, hippocampus, amygdala, perirhinal cortex, and entorhinal cortex.

Highlights

- The allocentric medial temporal lobe network is globally efficient, with no main hub
- Ventral visual stream plays a particularly central role in the allocentric network
- Allocentric representations are in distinct but neighboring neural populations
- The human brain encodes both scaled and true Euclidean representations

Evensmoen et al., 2021, Cell Reports *34*, 108658
January 19, 2021
https://doi.org/10.1016/j.celrep.2020.108658

CellPress

Cell Reports

CellPress
OPEN ACCESS

Article

Allocentric representation in the human amygdala and ventral visual stream

Hallvard Røe Evensmoen,[1,6,8,*] Lars M. Rimol,[2] Anderson M. Winkler,[3] Richard Betzel,[4] Tor Ivar Hansen,[1] Hamed Nili,[5] and Asta Håberg[1,6,7]

[1]Department of Neuromedicine and Movement Science, Norwegian University of Science and Technology (NTNU), 7489 Trondheim, Norway
[2]Department of Psychology, NTNU, 7489 Trondheim, Norway
[3]National Institutes of Health, 9000 Rockville Pike, Bethesda, MD 20892, USA
[4]Department of Psychological and Brain Sciences, Indiana University Bloomington, Bloomington, IN, USA
[5]Department of Experimental Psychology, University of Oxford, South Parks Road, OX1 3UD Oxford, UK
[6]Department of Medical Imaging, St. Olav's Hospital, Trondheim University Hospital, Trondheim, Norway
[7]Department of Circulation and Medical Imaging, NTNU, Trondheim, Norway
[8]Lead contact
*Correspondence: hjernemannen@gmail.com
https://doi.org/10.1016/j.celrep.2020.108658

SUMMARY

The hippocampus and the entorhinal cortex are considered the main brain structures for allocentric representation of the external environment. Here, we show that the amygdala and the ventral visual stream are involved in allocentric representation. Thirty-one young men explored 35 virtual environments during high-resolution functional magnetic resonance imaging (fMRI) of the medial temporal lobe (MTL) and were subsequently tested on recall of the allocentric pattern of the objects in each environment—in other words, the positions of the objects relative to each other and to the outer perimeter. We find increasingly unique brain activation patterns associated with increasing allocentric accuracy in distinct neural populations in the perirhinal cortex, parahippocampal cortex, fusiform cortex, amygdala, hippocampus, and entorhinal cortex. In contrast to the traditional view of a hierarchical MTL network with the hippocampus at the top, we demonstrate, using recently developed graph analyses, a hierarchical allocentric MTL network without a main connector hub.

INTRODUCTION

Mental representation of the external environment without reference to self-position, or allocentric representation, is critical for our way-finding ability (O'Keefe and Conway, 1978; Tolman, 1948). It has long been a goal of neuroscientific research to identify the brain structures involved in allocentric representation and understand how these structures interact (Ekstrom et al., 2014, 2017; Epstein et al., 2017). An allocentric representation contains viewpoint-independent information on spatial locations—in other words, it contains the positions of landmarks or objects in relation to each other, in contrast to an egocentric representation, which contains the positions of landmarks relative to the navigator (O'Keefe and Conway, 1978). Allocentric *positional patterns* of objects form two-dimensional (2D) overviews of the surrounding environment and are fundamental components of cognitive maps. It is not known where in the human brain cognitive maps are generated and stored (Ekstrom et al., 2017), nor whether the brain uses actual world geometry (i.e., accurate distances and angles between object positions—"Euclidean metrics") when constructing such maps.

The hippocampus and entorhinal cortex are considered the primary brain regions for allocentric representation in rats and humans (Ekstrom et al., 2014; Epstein et al., 2017; Evensmoen et al., 2015). However, it is an open question whether and to what extent other parts of the medial temporal lobe (MTL) subserve this function. A virtual navigation study in monkeys revealed that neuronal activity in a part of the ventral visual stream called the parahippocampal cortex (PHC) (Rosenke et al., 2018) conveyed more information about spatial location than activity in other MTL structures (Furuya et al., 2014), suggesting that the ventral visual stream is critically involved in spatial processing in primates. Human lesion studies have linked the PHC to recall of the positions of objects in the environment (Bohbot et al., 1998; Kolarik et al., 2016, 2018). Furthermore, an fMRI study showed increased PHC activation when a central landmark was used to remember spatial locations (Zhang and Ekstrom, 2013), and similarity between fMRI activation patterns in the PHC and hippocampus has been linked to map-drawing performance (across subjects) (Stokes et al., 2015). Moreover, rats with perirhinal lesions have been shown to use a primarily non-allocentric navigation strategy (Ramos, 2017), suggesting that the perirhinal cortex may also play a role in allocentric representation. The PHC and perirhinal cortex are strongly connected to both hippocampal place cells and entorhinal grid cells in rodents as well as humans (Burke et al., 2018). Finally, the amygdala, well known for its role in emotional processing (LaBar and Cabeza, 2006), has a high percentage of place-responsive cells in

humans, as seen in Figure S4 in Jacobs et al. (2010), suggesting that it has a role in spatial processing as well. These findings point toward possible roles in spatial processing for various MTL structures outside the hippocampal-entorhinal circuit. Here, we demonstrate that accurate allocentric representation is subserved by multiple MTL structures, including the hippocampus and the entorhinal cortex, as well as the amygdala, perirhinal cortex, and ventral visual stream structures.

RESULTS

Assessment of environmental encoding

To investigate allocentric representation in the human MTL, we acquired high-resolution fMRI (1.9 mm isotropic) data while healthy, right-handed young men freely explored 35 unique virtual environments (rooms), each of which contained 5 objects that were placed inside the room in a unique positional (spatial) pattern. The participants had 30 s to explore the room, followed by a 15-s "post-exploration period" with a fixation cross on the screen, in which they were free to engage in non-stimulus-driven encoding (Figure 1A) (Cohen et al., 2015). After every five rooms, the participants were tasked with dragging and dropping the objects from each room into a 2D overview representation of the room (Figure 1B). During these tests (seven in total) there was no fMRI BOLD (blood oxygen level-dependent imaging) scanning. The behavioral data collected in these tests were used as explanatory variables in the subsequent fMRI analyses.

To assess the accuracy of environmental encoding, the responses to the drag-and-drop task were quantified and three measures of allocentric accuracy (1–3) were obtained, all three of which were based on the "positional pattern" of the objects in the room (i.e., the angles and distances between them, regardless of the identities of the objects) (Figure 1C). (1) Pattern accuracy represents the accuracy of the positional pattern of objects, after correcting for rotation and translation (relative to the correct positional pattern) using the Kabsch algorithm (Kabsch, 1976), as well as up or down scaling of the positional pattern, minimizing the root mean square deviation from the correct positional pattern (Horecka et al., 2018; Umeyama, 1991) (see Method details). Scaling was done because spatial representations in humans are often scaled up or down (i.e., either compressed or expanded) (Horecka et al., 2018; Spiers et al., 2001; Tversky, 1992). The encoded positional patterns of objects were on average scaled up (expanded) by a factor of 1.11 ± 0.06, rotated $-0.48^{\circ} \pm 2.1^{\circ}$, and translated 0.84 ± 0.2 absolute virtual meters, relative to the correct positional pattern. After translation, rotation, and scaling, the positions provided by the participants were on average 0.75 ± 0.17 absolute virtual meters from the correct positions; before translation, rotation, and scaling, the positions were off by 1.32 ± 0.33 absolute virtual meters. (2) Environmental geometry is the degree to which the positional pattern is correct relative to the room's outer perimeter (the walls). Environmental geometry is defined as the inverse of the degree of translation, rotation, and scaling performed to obtain Pattern accuracy, and thus a high environmental geometry score, implies low degrees of rotation, translation, and scaling, relative to the room's walls. (3) Euclidean map is defined such that a high score reflects "high scores on both pattern accuracy and environmental geometry." A Euclidean map constitutes a cognitive map of the environment, including its outer perimeter; however, it does not take into account the identity of the objects. Finally, recall of which object was located in which position was also measured, and this is termed (4) object identity. The participants remembered on average 1.24 ± 0.15 objects correctly per environment (Figure S1A). Importantly, the present approach allows us to conduct a complete study of the components of allocentric representation, in contrast to previous fMRI studies, which typically limited the analyses to singular aspects of allocentric representation, such as direction of movement (Bellmund et al., 2016; Chadwick et al., 2015; Deuker et al., 2016) or the distance between pairs of landmarks (Deuker et al., 2016; Hirshhorn et al., 2012; Kyle et al., 2015; Morgan et al., 2011; Nau et al., 2020; Nielson et al., 2015).

Different levels of recall accuracy

To identify neural substrates of allocentric representation, it was necessary to find MTL regions that showed consistent modulation of fMRI activation patterns across different levels of allocentric accuracy. For this purpose, recalled positional patterns were compared to the correct positional patterns and classified as having either "fine" (high), "medium," or "coarse" (low) allocentric accuracy. These three categories were later used as levels of accuracy in multivariate fMRI analyses of activation pattern dissimilarity. Trials with accuracy at or below chance level were categorized as "failed." Chance level was defined by finding the cutoff point between two distributions while maximizing sensitivity and specificity (Figure S1). The first distribution was that of the actual accuracy scores, the recalled positional pattern compared to the correct positional pattern, across all participants and environments; the second distribution contained comparisons between the recalled positional pattern and the correct patterns from all of the other environments, across all of the participants. For pattern accuracy and environmental geometry, the thresholds between fine, medium, and coarse trials were defined such that, across participants, the average number of trials was the same for all three categories. For the Euclidean map, the average pattern accuracy score between fine Euclidean map and fine pattern accuracy was not different ($w = 241$, $p = 0.2$), and the average environmental geometry score between fine Euclidean map and fine environmental geometry also not different ($w = 249$, $p = 0.2$).

Allocentric positions and object identity are encoded by separate neural populations

Increased dissimilarity of neural activation patterns has been associated with more accurate encoding (Alm et al., 2019; Chanales et al., 2017; Copara et al., 2014; Favila et al., 2016; Jenkins and Ranganath, 2016; Koolschijn et al., 2019; LaRocque et al., 2013), and reduced memory interference has been suggested to be the underlying mechanism for this (Brunec et al., 2020; Clewett et al., 2019; Favila et al., 2016). We therefore wanted to find out whether increased allocentric accuracy during environmental encoding was associated with more dissimilar fMRI activation patterns in the MTL. For this purpose, we used a reliable multivoxel representational similarity analysis (RSA) (Figure S2A) (Kriegeskorte and Bandettini, 2007; Kriegeskorte et al., 2006; Nili

CellPress
OPEN ACCESS

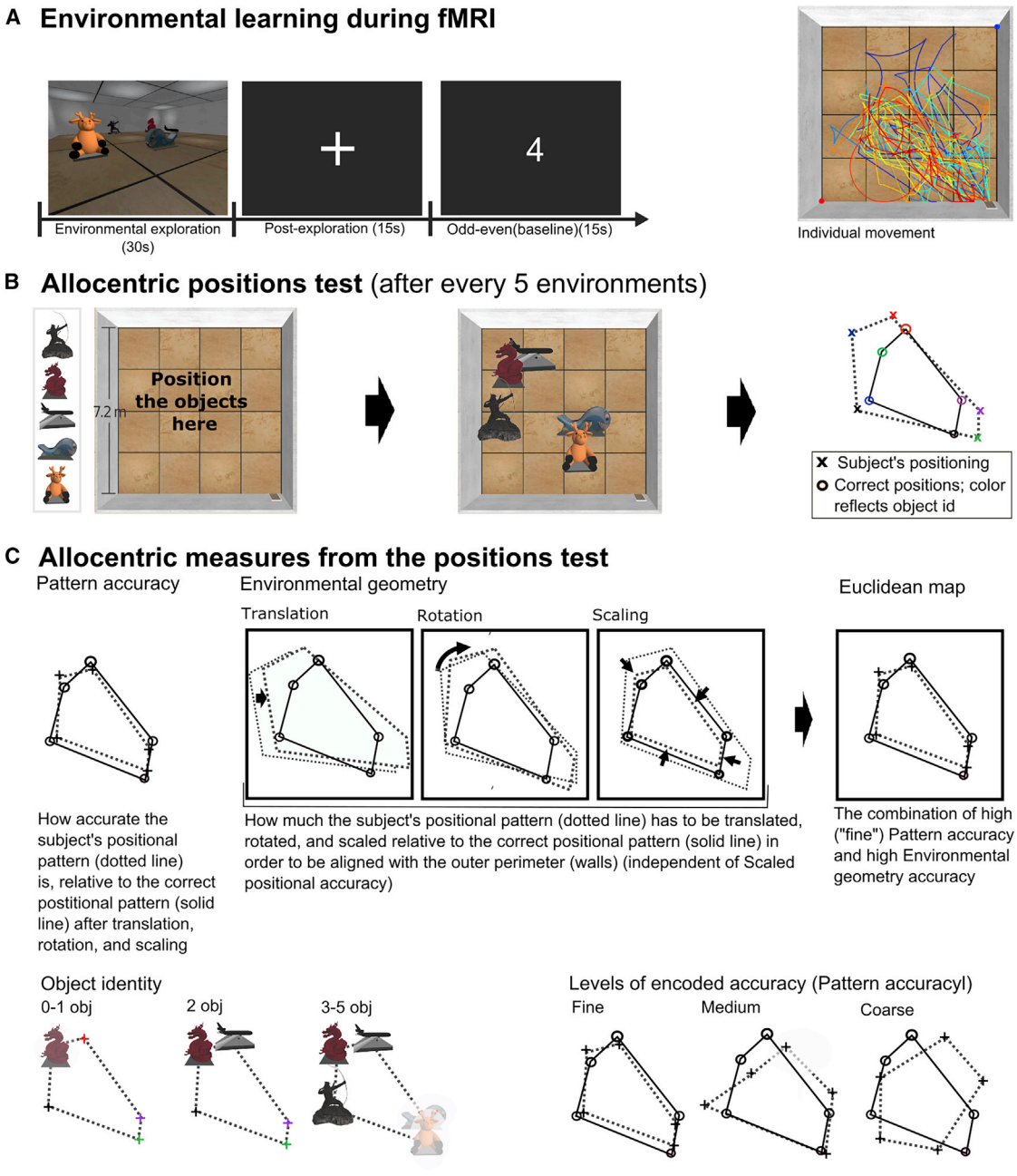

Figure 1. The fMRI paradigm and assessment of environmental encoding

(A) Left: the fMRI paradigm involved free exploration of the environment from a first-person perspective using a joystick to move around (environmental exploration), followed by a post-exploration encoding period while fixating on a cross, and, subsequently, an odd-even judgment task (baseline). Right: the individual movement of all participants (differently colored lines for each participant) in one of the environments.

(B) After 5 environments had been presented, the participant's recall was evaluated. Left: in the allocentric positions test, the participant viewed the environment from a 2D overview and was asked to drag and drop the objects into their correct locations using the joystick. Right: an actual response from one of the participants, with colors indicating object identity.

(C) Assessment of participant responses: Top row, left: pattern accuracy reflects the degree to which the relative positions of the objects (their positional pattern) were correctly recalled, when object identity is disregarded and the pattern has been translated, rotated, and scaled relative to the correct positional pattern. Center: environmental geometry reflects the degree to which the positional pattern, as recalled by the participant, had to be rotated, translated, and scaled to perfectly align with the outer wall (independent of pattern accuracy). Right: Euclidean map reflects the degree to which the participant's response displayed a high degree of pattern accuracy as well as high environmental geometry (see Method details). Bottom row, left: object identity reflects how many objects were recalled in their correct positions within the positional pattern (independent of pattern accuracy). Right: examples of high ("fine"), medium ("medium"), and low ("coarse") accuracy responses. See also Figure S1.

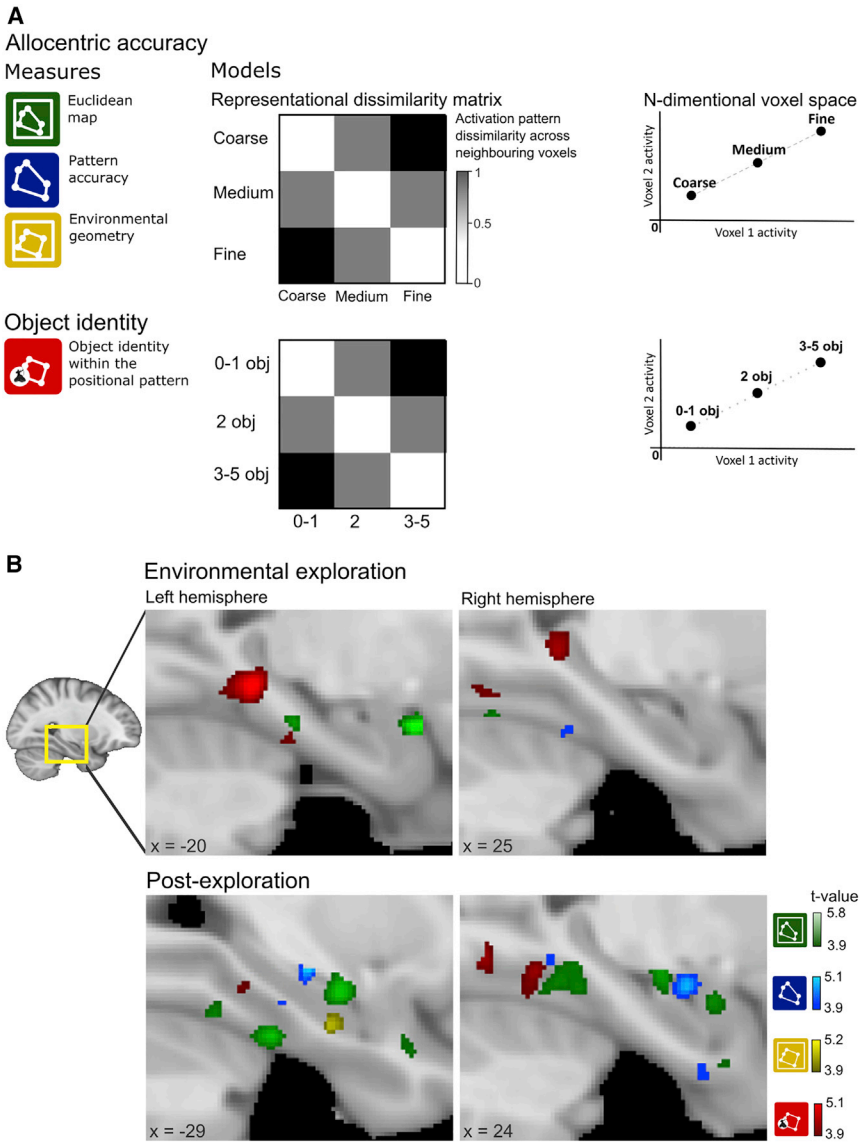

Figure 2. Allocentric accuracy and object identity encoded in separate neural populations

(A) Left column: the measured allocentric variables, Euclidean map (green), pattern accuracy (blue), environmental geometry (yellow), and object identity (i.e., number of objects correctly placed within positional pattern [red]). Right column: the statistical model used to test for allocentric accuracy. Of note, the model predicts a consistent modulation of activation pattern dissimilarity with increasing encoding accuracy.

(B) Medial temporal lobe voxels that showed consistent modulation of activation pattern dissimilarity as allocentric encoding became more accurate (from coarse via medium to fine) (green, blue, and yellow) or as more objects were correctly placed (red). Subsequent analyses revealed that allocentric accuracy was associated with increasingly unique brain activation (see Results). Results are shown for environmental exploration (top row) and post-exploration (bottom row). Permutation-based cluster mass corrected thresholds of $p < 0.05$ were used, taking into account both the size of the clusters and the size of the voxel-wise activations within the clusters. The "x =" in the lower left corner of each brain image indicates the sagittal position in MNI space.

See Figure S2, Table S1, and Table S2 for more details on activation locations, and Table S4 for activation pattern dissimilarity-based classification.

et al., 2014; Walther et al., 2016), including a multivariate noise normalization that corrects for noise-related co-variance across voxels (Walther et al., 2016), such as a set of voxels being supplied by the same artery. For each voxel in the MTL, a 4-mm-radius sphere ("searchlight") was defined, with the target voxel as the center. An initial univariate general linear model (GLM) analysis was used to extract the univariate activation for every voxel within the sphere for each of the three levels of accuracy (coarse, medium, and fine). Thus, for each level of accuracy, there was an associated activation pattern—distribution of univariate activations (betas from the GLM)—within the sphere. The RSA analysis tested whether the activation patterns became more or less similar with increasing allocentric accuracy (Figures 2A and S2A) and revealed that activation pattern dissimilarity throughout the MTL was consistently modulated by the increasing level of pattern accuracy (from coarse to medium to fine) (Figures 2B and S2B; Tables S1 and S2). These findings are consistent with multiple MTL regions being specialized for allocentric representation. Similar results were obtained for the Euclidean map. For environmental geometry, only the anterior hippocampus showed a consistent modulation with increased accuracy, and the effect was only observed in the post-exploration period. There were no effects for models in which medium accuracy was compared to fine and coarse, and we found no relationship between the correlation effects (i.e., activation pattern dissimilarities, from coarse to medium to fine), and average success rate across subjects. For object identity, activation pattern dissimilarity was consistently modulated by the increasing level of accuracy (from 0–1 to 2 to 3–5 objects recalled), in the same set of subregions as for pattern accuracy and Euclidean map. The only exception to this was the amygdala (Figures 2 and S2B; Tables S1 and S2). Finally, the positional pattern representation for allocentric representations was located to the posterior medial entorhinal cortex and medial perirhinal cortex, while object identity was primarily located in the anterior lateral entorhinal cortex and lateral perirhinal cortex. The divisions of the entorhinal and perirhinal cortices into anterior/posterior and lateral/medial regions were made by an experienced neuroanatomist and based on finding the central Montreal Neurological Institute (MNI) coordinates along the

anterior-posterior and lateral/medial axes (see Method details). The present findings support the hypothesis that the perirhinal cortex is functionally segregated into a medial (area 35) and a lateral (area 36) component (Burke et al., 2018). The present results show that allocentric and object identity representations are encoded in a widespread network of distinct but neighboring neural populations throughout the MTL. Leave-one-subject-out cross-validated nearest-neighbor classifiers, trained on the activation pattern dissimilarities for peak regions of interest (ROIs) from the RSA analyses (Euclidean map, pattern accuracy, environmental geometry, and object position), showed an average classification accuracy of 0.83 ± 0.26 for the classes from the model activation pattern dissimilarity matrix (RDM) (Table S4), confirming the validity of the RSA results.

Our findings show that activation pattern dissimilarity associated with allocentric MTL processing is consistently modulated by increasing levels of accuracy. One possible explanation is that the accurate (“fine “) trials drive the increases in activation pattern dissimilarity; another possibility is that the least accurate (“coarse”) drive increases in dissimilarity. To resolve this ambiguity, we used RSA analyses that allowed dissimilarity comparisons between “fine” and baseline (last 5 s of odd-even) and “coarse” and baseline. The results showed that “fine” displayed significantly larger dissimilarity between its activation patterns and baseline than “coarse” did between its activation patterns and baseline (Table S3), indicating that increased dissimilarity is driven by “fine” trials. Conversely, for object identity, the least accurate or failed trials (0–1 object remembered) showed higher degrees of dissimilarity compared to baseline.

The allocentric MTL network is hierarchical with three main modules

To assess connectivity between the MTL regions found to be involved in environmental encoding, we performed a high-reliability multivariate distance correlation analysis (Geerligs et al., 2016) combined with state-of-the-art graph theory (Figure 3A) (Jeub et al., 2018). The peak voxels from the RSA analyses of environmental encoding, consisting of data from four separate GLMs (Figure 2A), were used to select functional ROIs. The ROIs are listed in Figure 3 and include subregions within the PHC, perirhinal cortex, hippocampus, entorhinal cortex, amygdala, and the fusiform gyrus, which is part of the ventral visual stream. The multivariate distance correlation analysis showed that all subregions were significantly connected with each other during both the environmental exploration and the post-exploration periods (Figure 3B). This means that the subregions showed a similar change in activation pattern dissimilarity from one trial to the next throughout the experiment (Basti et al., 2020; Geerligs et al., 2016; Ritchey et al., 2014; Stokes et al., 2015) (see Method details).

A multiresolution consensus clustering analysis based on graph theory starts with all of the nodes belonging to the same module, then searches for pairwise co-classifications of the nodes and, where significant co-classifications exist, divides the original module into sub-modules at ever more fine-grained levels, until no more significant sub-modules are found. This process is based on the strength of the connections between the nodes and enables detection of a hierarchy of nested modules across levels (Jeub et al., 2018) (see Figure 4). This analysis revealed that the nodes of the allocentric network formed a dynamic hierarchical connectivity structure with three (bilateral) top-level (main) modules that changed from the environmental exploration to the post-exploration period (Figure 4). This hierarchical structure appeared to be preserved at an individual level (Figures S3C and S3D). All of the top-level modules supported the encoding of object identity and pattern accuracy and/or Euclidean map, except for a posterior-medial entorhinal and PHC module in the post-exploration period, which supported only pattern accuracy and Euclidean map. The entorhinal cortex was in a module separate from the hippocampus and the parahippocampal cortex for the environmental exploration period (magenta module in Figure 4), even though the entorhinal cortex shares strong anatomical connections with both structures (Burke et al., 2018; Ritchey et al., 2015). This is consistent with brain connectivity being dynamic and optimized for the task at hand (Bassett et al., 2011; Braun et al., 2015; Cole et al., 2014; Saggar et al., 2018; Schedlbauer and Ekstrom, 2019; van den Heuvel and Sporns, 2013) and, moreover, suggests that models for allocentric representation based solely on structural (anatomical) connections within the MTL are inadequate. Furthermore, no singular subregion was part of all of the modules for the environmental exploration period, but the fusiform cortex, hippocampus, PHC, and perirhinal cortex were part of two out of the three main modules. In the post-exploration period, the PHC was the only subregion that was part of all of the modules. All in all, these observations indicate that the allocentric MTL network is characterized by three main modules that change with the task at hand and are not linked together by any singular MTL region. Stability analyses using a leave-one-subject-out approach revealed that the top-level partitions with one subject missing consistently were identical to the top-level partition when data from all of the subjects were used. Similarly, the top-level partitions using a “leave-one-trial-out” approach were identical to the top-level partition when using data from all of the trials for the environmental exploration period, and highly similar for the post-exploration period, with an average overlap of 93% ± 11% (based on the adjusted Rand similarity coefficient), which confirms the validity of our connectivity analyses.

The allocentric MTL network contains several central nodes with no connector hub

If a single brain structure, such as the hippocampus, sits atop an allocentric processing hierarchy in the MTL, then we would expect it to receive information from all of the other MTL structures and act as a connector hub. A connector hub has both a higher degree of centrality (degree centrality and betweenness centrality) and a higher degree of connectivity across modules (participation coefficient) than other nodes, indicating that it links nodes from different modules to each other (Rubinov and Sporns, 2010; van den Heuvel and Sporns, 2013). We tested this hypothesis by applying graph analysis (see Method details) to the multivariate distance correlation matrix. We did not find a singular brain structure (node) with a higher degree centrality (i.e., a higher number of connections) or participation coefficient (i.e., a larger number of connections across main modules) than all of the other nodes in the network (Rubinov

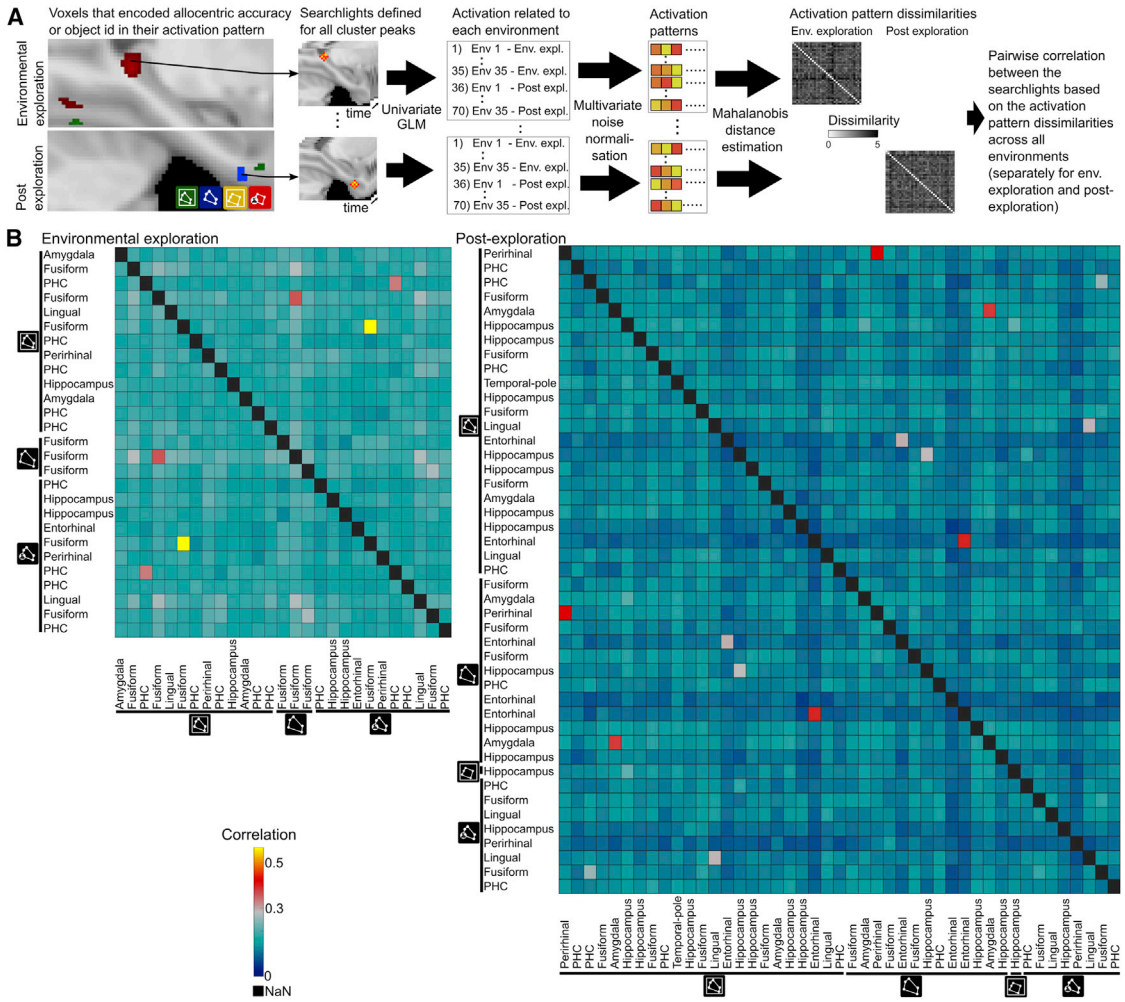

Figure 3. The allocentric MTL network

(A) A searchlight was defined for each medial temporal lobe (MTL) voxel that showed a local peak effect for pattern accuracy, environmental geometry, Euclidean map, or object identity encoding. The searchlights were grouped together based on whether the peak voxel originated from the environmental exploration or the post-exploration period, to establish separate MTL networks for environmental exploration and post-exploration. For each searchlight, the voxel-wise activation was estimated for every environment using a univariate GLM, followed by a multivariate noise normalization of the (multivoxel) activation patterns. The activation pattern dissimilarities between all of the environments were then calculated, resulting in one activation pattern dissimilarity matrix for each searchlight. Now, functional connectivity could be estimated between the searchlights by computing the pairwise correlation (Kendall's τ) between the activation pattern dissimilarity matrices. The functional connectivity thus reflects to what extent the MTL structures showed a similar change in activation pattern dissimilarity from one environment to another throughout the experiment.

(B) Average correlation (Kendall's τ) across all of the subjects and between functional regions of interest, from the allocentric encoding analyses, for the environmental exploration (left column) and post-exploration (right column). A 2-sided Wilcoxon signed rank test showed that there was significant correlation, indicating functional connectivity, between all of the nodes in the allocentric MTL network, using a threshold corresponding to $p < 0.05$ (false discovery rate [FDR] corrected).

and Sporns, 2010) (Figure 5; Tables S5 and S6). For betweenness centrality, we did find a larger number of shortest communication paths between other nodes passing through the temporo-occipital fusiform cortex than the other nodes in the MTL network (Rubinov and Sporns, 2010) (Tables S5 and S6); however, there was no singular structure (node) consistently demonstrating higher betweenness centrality, degree centrality, and participation coefficient than other nodes in the network. These findings demonstrate that allocentric representation is not completely encoded in one specific MTL region, but rather is an emergent property of a network comprising a set of core regions within the MTL. Consistent with this, associations between behavioral performance and global graph measures were significant between pattern accuracy and global allocentric network efficiency (Figure 6; Table S7), concordant with previous studies demonstrating a relationship between task performance and global efficiency of task-related brain networks (Bullmore and Sporns, 2012). Global efficiency is defined as the average inverse shortest path length between every pair of nodes in the network, and is a measure of the

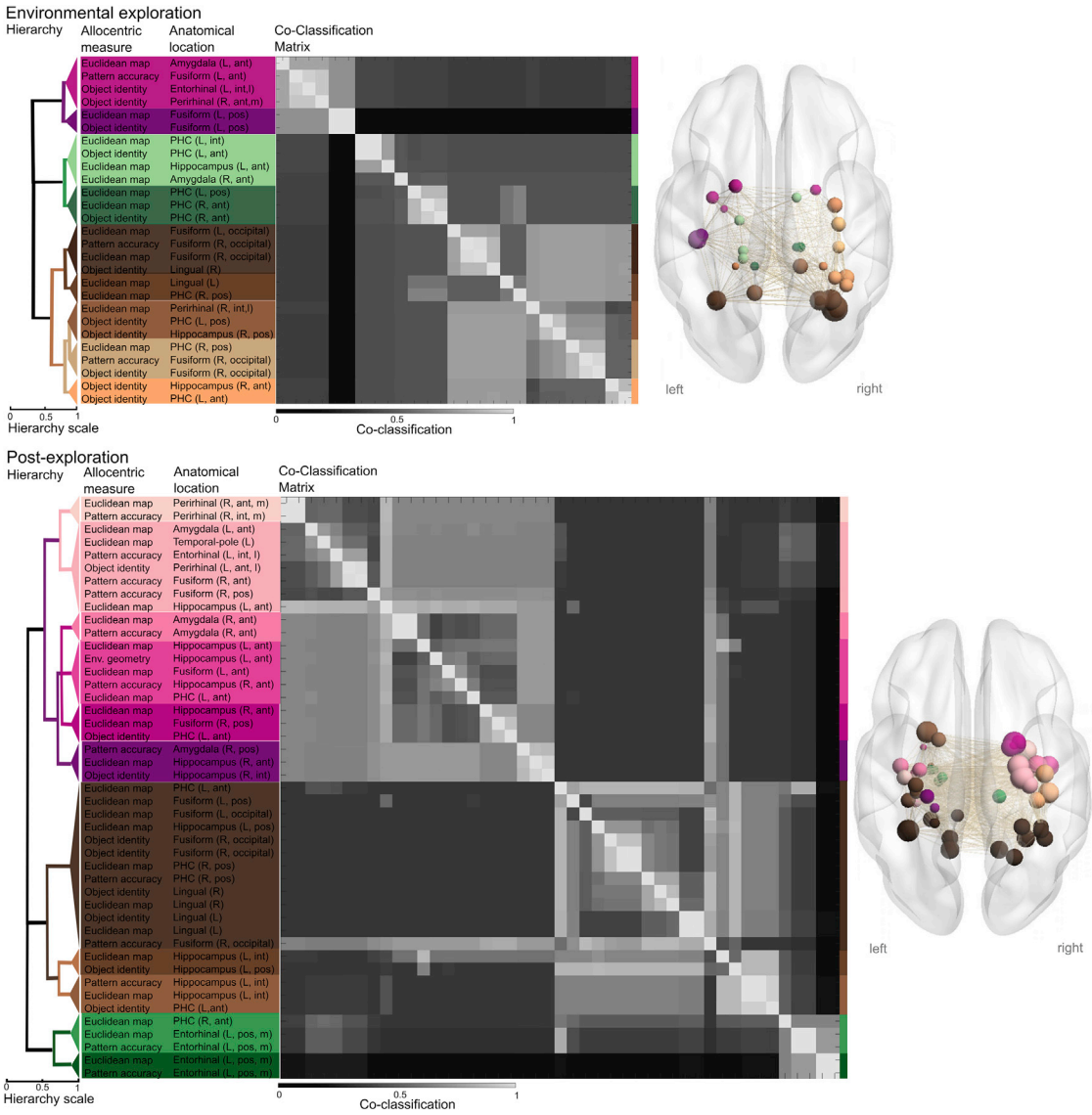

Figure 4. The allocentric MTL network is hierarchical

Left: a multiresolution consensus clustering analysis of the functional connectivity data revealed a hierarchical allocentric MTL network with 3 (anterior-posterior) top-level (main) modules (magenta, green, and brown) for the environmental exploration period (top row) and the post-exploration period (bottom row). The anatomical locations are functional peaks from the different allocentric features and object identity encoding analyses (4 separate GLMs). The multiresolution clustering analysis starts with the assumption that all of the nodes belong to the same module. It then divides this module into sub-modules at ever more fine-grained levels, based on significant pairwise co-classification of the nodes, enabling detection of a hierarchy of nested modules across levels.

Right: the MTL nodes overlaid on an MNI template of the brain. All of the branches of the tree were significant, with a threshold of $p < 0.05$.

See also Figure S3.

overall capacity of the network to transfer information in parallel (Bullmore and Sporns, 2012).

DISCUSSION

We demonstrate here allocentric representation in distinct neural populations in the human MTL of healthy young men, including structures not predicted by existing models (Ekstrom et al., 2014, 2017; Epstein et al., 2017), such as the fusiform gyrus (ventral visual stream), amygdala, and perirhinal cortex. These structures, together with the parahippocampal cortex, the hippocampus, and the entorhinal cortex, comprise an extensive MTL network for allocentric representation. Contrary to the classical models, we found no evidence that the hippocampus is a main (connector) hub within the hierarchical allocentric MTL network, suggesting that allocentric encoding originates from a network of closely linked nodes, rather than an individual brain region.

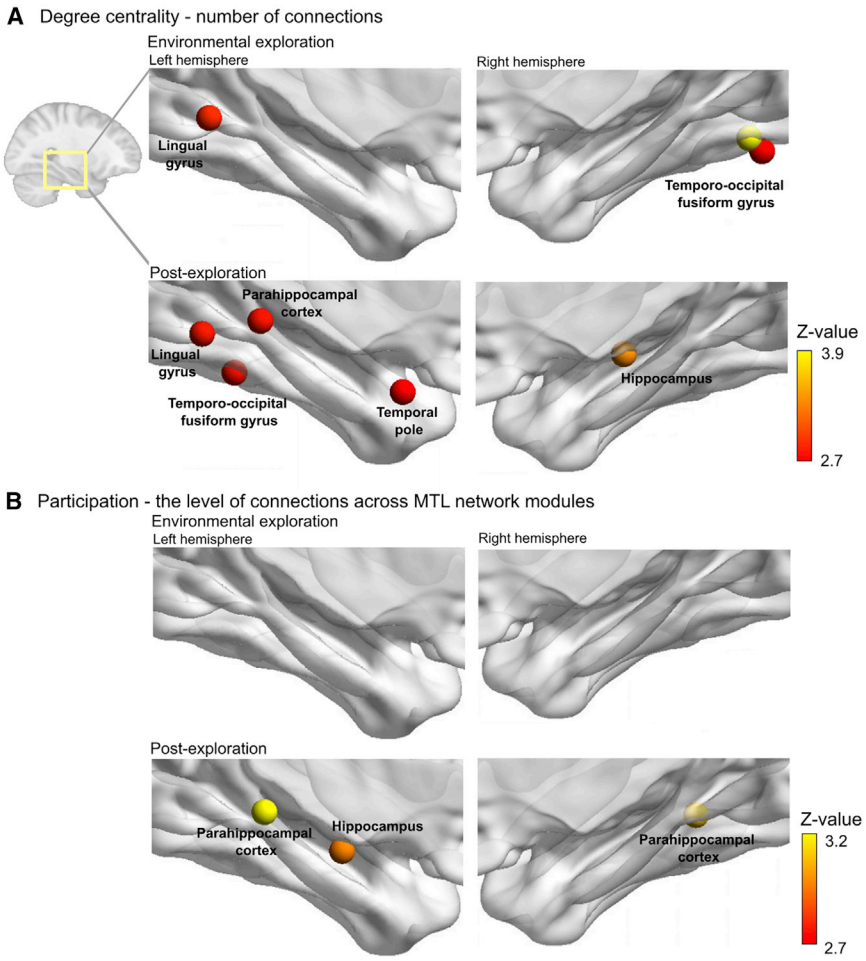

Figure 5. The allocentric MTL network includes several central nodes

(A) The spheres represent nodes with a significantly higher number of connections than the other nodes (degree centrality) in the allocentric MTL network (see also Tables S5 and S6). A lighter node color indicates higher degree centrality.

(B) The level of connections across network modules (participation) for each node in the allocentric MTL network (see also Tables S5 and S6 and Figure S3). A lighter color indicates higher participation rate. Both degree centrality and participation were estimated across subject-specific allocentric MTL networks. Importantly, there was no significant variation in temporal signal-to-noise ratios across the MTL nodes in the environmental exploration period, and there was no relationship between temporal signal-to-noise ratio and degree centrality or participation (Table S8). A FDR-corrected significance level of $p < 0.05$ was used.

The fusiform gyrus was the only structure in the allocentric MTL network with an increased number of shortest communication paths passing through it, and the parahippocampal cortex the only MTL structure with a node that showed both a high degree of centrality and a high degree of connectivity across modules. The fusiform gyrus and the parahippocampal cortex are parts of the ventral visual stream (Rosenke et al., 2018) and specific to primates (the fusiform gyrus exists only in hominoids) (Ekstrom, 2015; Weiner and Zilles, 2016). Primates define where they are based on what they see, using their advanced visual system and spatial view cells that encode space within an allocentric framework (Rolls and Wirth, 2018), which is consistent with the notion that the human ability to use small-scale maps depends on a high-resolution visual system (Ekstrom, 2015). Mammals with less evolved visual systems, such as rodents (Kaas, 2005), define where they are based on where they are located using for example their whiskers (Rolls and Wirth, 2018). In rodents, there is no parahippocampal cortex but in the postrhinal cortex, a structure with similar connectivity to the parahippocampal cortex (Burwell, 2001); a small proportion of cells have coarse place fields that seem to support perceptual rather than mnemonic functions (Burwell and Hafeman, 2003). In primates, as cortical areas became larger over the course of evolution, and acquired more neurons, processing likely transitioned from global to local comparisons, i.e., neurons with specific response properties were grouped with adjoining groups of functionally related neurons, leading to modular computations of input (Kaas, 2005). We speculate that the postrhinal cortex in rodents evolved into specialized modules for accurate allocentric representation in modern primates. Thus, the evolutionary expansion of primate temporal lobes, together with the highly evolved primate visual systems, may have provided the ventral visual stream with a crucial role in allocentric representation in humans.

A recent study in rodents showed that post-training stimulation of the pathway from the amygdala to the medial entorhinal cortex enhanced the retention of spatial memories in a Barnes's maze, but did not affect foot shock learning (Wahlstrom et al., 2018). This suggests that, although the amygdala is important for emotional memory, including foot shock learning (LaBar and Cabeza, 2006), there may be at least one amygdala pathway uniquely involved in spatial memory. In humans, an intracranial electroencephalogram (EEG) study found place cells in the amygdala that fire when the subject occupies specific spatial locations, but no "path cells," cells that fire in response to a specific path chosen through an environment (Jacobs et al., 2010; Miller et al., 2013). It should be noted that place cell firing does not prove allocentric processing (Ekstrom et al., 2014); however, in contrast to these previous studies, our findings clearly demonstrate that in humans, the amygdala is involved in allocentric representation of positional patterns.

A long-held view has been that allocentric representation emerges within a hierarchical MTL network, in which different components are processed separately and then added together in the hippocampus to form a cognitive map (Banta Lavenex

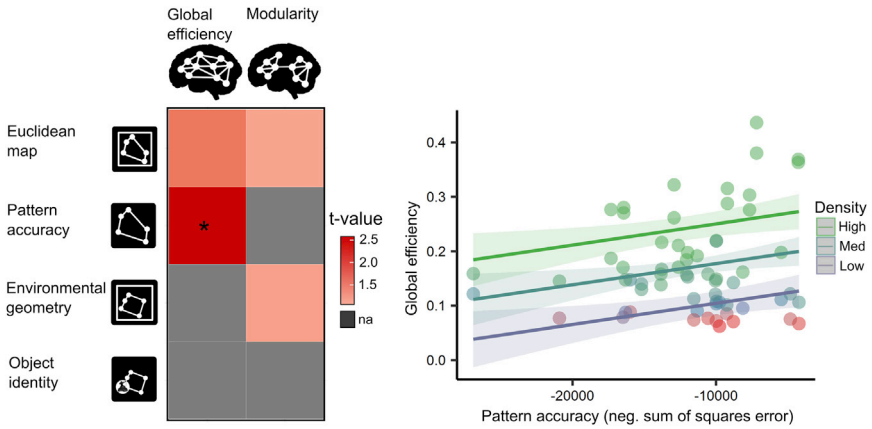

Figure 6. Global efficiency in the allocentric MTL network is related to encoded allocentric accuracy

Left: mixed linear model analyses showed that increased global efficiency of the allocentric network is associated with more accurate encoding of the objects' positional patterns (pattern accuracy) across participants. Global efficiency is a measure of the network's overall capacity to transfer information in parallel (Bullmore and Sporns, 2012), while modularity was defined as the number of top-level (main) modules in the allocentric MTL network. Right: the predicted values (marginal effects) with 95% confidence intervals for pattern accuracy (line plots) in the model, with global efficiency as the dependent variable, while controlling for network density. Density is the number of connections present in the network divided by the total possible number of connections. The dots represent raw data points. *$p < 0.05$ (FDR corrected); "na" indicates that the measure did not explain individual variance in global efficiency or modularity.

See also Table S7 and Figure S3.

et al., 2014; Ritchey et al., 2015). This view is based on the major anatomical connections established in primates (Aggleton, 2012) and resting-state fMRI studies in humans (Ritchey et al., 2015). It proposes that the PHC and the posterior medial entorhinal cortex form a positional information pathway, whereas the perirhinal cortex and the anterior lateral entorhinal cortex form an object identity information pathway. Both pathways lead to the hippocampus, which "may serve as sites of integration between the two systems," together with the ventromedial prefrontal cortex (Ritchey et al., 2015). More recently, however, based on findings in rats, it has been argued that mental representations of objects and environmental positions are integrated in non-hippocampal MTL regions, including the perirhinal and entorhinal cortices (Connor and Knierim, 2017). Here, we show that in humans, objects and environmental positions are integrated in the perirhinal cortex, the PHC, the fusiform cortex, and to some extent the entorhinal cortex. Moreover, the largest effects for Euclidean map were not located in the hippocampus or the entorhinal cortex, previously described as likely to be the primary brain regions for "map-like spatial codes" in humans (Epstein et al., 2017), but in the perirhinal cortex, PHC, fusiform cortex, and the amygdala. The finding that core regions within the emotional and visual networks of the brain are also core regions in the allocentric network of the brain, together with the recent observation that activation patterns in the visual cortices are the best predictors of emotion category (Kragel et al., 2019), suggest that these three cognitive systems are more closely intertwined than previously believed.

Our network analyses demonstrated that the allocentric MTL network consists of nodes with a high degree of interconnectedness, and that most main modules in the network support encoding of object position and allocentric representations. This suggests that a successful allocentric representation emerges from "non-additive computations shared across multiple interacting brain regions" (Ekstrom et al., 2014, 2017; Huffman and Ekstrom, 2019), rather than being the product of activation in a single brain region. This is supported by selective hippocampal lesions in monkeys resulting in no robust memory impairment (Basile et al., 2020), as well as increased MTL connectivity for recall of episodic memories in humans (Geib et al., 2017; King et al., 2015; Schedlbauer et al., 2014; Westphal et al., 2017), including successful versus unsuccessful episodic retrieval (King et al., 2015; Schedlbauer et al., 2014). This stands in contrast to the traditional view of a hierarchical MTL network, with the hippocampus as the central node. Our findings show that object identity and positional representations are present in all main network modules except one, suggesting that allocentric information and object identity are integrated in multiple MTL structures, including but not limited to the hippocampus. Moreover, we found no connector hub in the allocentric MTL network. Rather, successful allocentric recall was associated with a high degree of global efficiency in the MTL network, supporting the idea that allocentric representation is an emergent property of the MTL network.

The anterior hippocampus was the only MTL structure that was associated with environmental geometry. Previous studies suggest that the posterior hippocampus is particularly important for learning the location of an object's position relative to a circular environmental boundary (Doeller et al., 2008), and that hippocampal place cells are attuned to the outer perimeter of the environment (O'Keefe and Burgess, 1996). Our findings demonstrate that one particular component of allocentric representation, environmental geometry, appears to depend primarily on the anterior hippocampus within the MTL network.

The posterior-medial entorhinal cortex was associated with Euclidean map and pattern accuracy, and the anterior-lateral entorhinal cortex with object identity and pattern accuracy. Previous fMRI studies have found allocentric representation in the posterior (medial) entorhinal cortex (Chadwick et al., 2015; Shine et al., 2019) and anterior entorhinal cortex (Shine et al., 2019). Only the anterior (lateral) entorhinal cortex has been involved in the representation of allocentric landmark direction (Shine et al., 2019) and localization based on landmarks (Chen et al., 2019). This indicates that the posterior-medial entorhinal cortex supports allocentric representation of positional patterns, while the anterior-lateral entorhinal cortex supports the linkage

of landmarks to (scaled) allocentric representations (in humans). This is consistent with findings in rodents showing multimodal integration in the anterior-lateral but not the posterior-medial entorhinal cortex (Doan et al., 2019). Moreover, we found that object identity representation was located more anterior and more lateral in the entorhinal cortex than any effect related to accurate representation of allocentric patterns. This suggests that representations become more landmark oriented, as well as less accurate, along the posterior-anterior and medial-lateral entorhinal axes, with no clear boundary between the posterior-medial and anterior-lateral entorhinal cortices.

It is well established that human spatial representation tends to be scaled down or up; in other words, distances between object landmarks may be compressed or expanded (Ekstrom et al., 2014; Horecka et al., 2018; Tversky, 1992). Conversely, for a representation to be Euclidean (representing actual world geometry), scaling must be absent or minimal. We report an average expansion of the encoded distances between objects (pattern accuracy) by a factor of ~1.1, similar to what was observed for a 2D spatial pattern (Horecka et al., 2018) and in accordance with geometrically inconsistent representation in humans (Warren et al., 2017). We also report activation associated with Euclidean representation (Euclidean maps) in separate, albeit neighboring, neural populations throughout the MTL. Associations between accurate positional representation and brain activation in the MTL have been reported (Baumann et al., 2010; Kyle et al., 2015), including a negative correlation between MTL activation and absolute metric error on a trial-by-trial basis (Baumann et al., 2010), as well as a positive correlation between MTL activation patterns associated with store-distance accuracy and classification accuracy in a virtual-city environment (Kyle et al., 2015). It has been suggested that the brain scales environmental information to construct an "environmental hierarchy" of encoded information, presumed to be conducive to efficient retrieval (Kim and Maguire, 2018; Tversky, 1992), but it is unclear why the brain supports both Euclidean and scaled positional representations.

The environments used in the present study were medium sized (50–90 virtual m^2), but they had no internal structural barriers and no connection to the outer world or other rooms, resulting in a relatively low level of complexity. We used environments of limited complexity to achieve maximal experimental control so as to enable the study of allocentric representation in isolation from confounding factors typically associated with complex environments, such as target or path planning, route selection, decision making, and brain activation associated with merging local parts of a larger environment (Wolbers and Wiener, 2014). Another important consideration was that the participants had to be able to learn the environment in <30 s, which is within the range of recommended block length for fMRI experiments (Wager and Nichols, 2003). Nevertheless, the limited complexity of these environments limits the generalizability of our findings to larger and more complex environments.

Our findings demonstrate that the human brain encodes scaled and true Euclidean representations in distinct but neighboring neural populations in the MTL of young men, including the fusiform cortex, the amygdala, and the perirhinal cortex. These structures were not predicted by existing models and appear to be part of a network of extensively connected, hierarchically organized MTL regions.

STAR★METHODS

Detailed methods are provided in the online version of this paper and include the following:

- KEY RESOURCES TABLE
- RESOURCE AVAILABILITY
  - Lead contact
  - Materials availability
  - Data and code availability
- EXPERIMENTAL MODEL AND SUBJECT DETAILS
  - Participants
- METHOD DETAILS
  - Image acquisition
  - fMRI paradigm
  - Tests between the runs
  - Measures of post-exploration accuracy
  - Post-experiment questionnaire
  - fMRI preprocessing
  - Regions of interest
- QUANTIFICATION AND STATISTICAL ANALYSIS
  - Behavioral data analysis
  - Activation pattern similarity analyses
  - Representational connectivity
  - Graph analysis
  - Temporal signal-to-noise ratio

SUPPLEMENTAL INFORMATION

Supplemental Information can be found online at https://doi.org/10.1016/j.celrep.2020.108658.

ACKNOWLEDGMENTS

We thank Jarle Ladstein for developing the fMRI sequence used and for helping with the data collection. We thank Kam Sripada and Henning Hoel Rise for valuable discussions and valuable input to the manuscript. We thank former master student Martin Sjøgård for helping out with establishing the RSA analyses. We thank Øyvind Salvesen for valuable discussions related to statistical analysis of the behavioral data. We also thank the staff at the Department of Medical Imaging at St. Olavs Hospital in Trondheim for assistance with imaging protocols and data acquisition. This work was supported by the Department of Neuromedicine and Movement Science, NTNU; Norwegian National Advisory Unit for fMRI.

AUTHOR CONTRIBUTIONS

H.R.E. designed the experiment, conducted the experiment, analyzed the data, and wrote the paper; L.M.R. contributed to the analysis of the data and the writing of the paper; A.M.W. contributed to the analysis of the data and the writing of the paper; R.B. contributed to the analysis of the data and the writing of the paper; T.I.H. contributed to the conduction of the experiment and the writing of the paper; H.N. contributed to the analysis of the data and the writing of the paper; and A.H. contributed to the design of the experiment and the writing of the paper.

DECLARATION OF INTERESTS

The authors declare no competing interests.

Received: September 30, 2019
Revised: October 1, 2020
Accepted: December 21, 2020
Published: January 19, 2021

REFERENCES

Aggleton, J.P. (2012). Multiple anatomical systems embedded within the primate medial temporal lobe: implications for hippocampal function. Neurosci. Biobehav. Rev. *36*, 1579–1596.

Alm, K.H., Ngo, C.T., and Olson, I.R. (2019). Hippocampal signatures of awake targeted memory reactivation. Brain Struct. Funct. *224*, 713–726.

Banta Lavenex, P.A., Colombo, F., Ribordy Lambert, F., and Lavenex, P. (2014). The human hippocampus beyond the cognitive map: evidence from a densely amnesic patient. Front. Hum. Neurosci. *8*, 711.

Basile, B.M., Templer, V.L., Gazes, R.P., and Hampton, R.R. (2020). Preserved visual memory and relational cognition performance in monkeys with selective hippocampal lesions. Sci. Adv. *6*, eaaz0484.

Bassett, D.S., Wymbs, N.F., Porter, M.A., Mucha, P.J., Carlson, J.M., and Grafton, S.T. (2011). Dynamic reconfiguration of human brain networks during learning. Proc. Natl. Acad. Sci. USA *108*, 7641–7646.

Basti, A., Nili, H., Hauk, O., Marzetti, L., and Henson, R.N. (2020). Multi-dimensional connectivity: a conceptual and mathematical review. Neuroimage *221*, 117179.

Bates, D., Mächler, M., Bolker, B., and Walker, S. (2015). Fitting linear mixed-effects models using lme4. J. Stat. Softw. *67*. https://doi.org/10.18637/jss.v067.i01.

Baumann, O., Chan, E., and Mattingley, J.B. (2010). Dissociable neural circuits for encoding and retrieval of object locations during active navigation in humans. Neuroimage *49*, 2816–2825.

Bellmund, J.L.S., Deuker, L., Navarro Schröder, T., and Doeller, C.F. (2016). Grid-cell representations in mental simulation. eLife *5*, e17089.

Bohbot, V.D., Kalina, M., Stepankova, K., Spackova, N., Petrides, M., and Nadel, L. (1998). Spatial memory deficits in patients with lesions to the right hippocampus and to the right parahippocampal cortex. Neuropsychologia *36*, 1217–1238.

Braun, U., Schäfer, A., Walter, H., Erk, S., Romanczuk-Seiferth, N., Haddad, L., Schweiger, J.I., Grimm, O., Heinz, A., Tost, H., et al. (2015). Dynamic reconfiguration of frontal brain networks during executive cognition in humans. Proc. Natl. Acad. Sci. USA *112*, 11678–11683.

Brock, G., Pihur, V., Datta, S., and Datta, S. (2008). clValid: An R Package for Cluster Validation. J. Stat. Softw. *25*. https://doi.org/10.18637/jss.v025.i04.

Brunec, I.K., Robin, J., Olsen, R.K., Moscovitch, M., and Barense, M.D. (2020). Integration and differentiation of hippocampal memory traces. Neurosci. Biobehav. Rev. *118*, 196–208.

Bullmore, E., and Sporns, O. (2012). The economy of brain network organization. Nat. Rev. Neurosci. *13*, 336–349.

Bullmore, E.T., Suckling, J., Overmeyer, S., Rabe-Hesketh, S., Taylor, E., and Brammer, M.J. (1999). Global, voxel, and cluster tests, by theory and permutation, for a difference between two groups of structural MR images of the brain. IEEE Trans. Med. Imaging *18*, 32–42.

Burke, S.N., Gaynor, L.S., Barnes, C.A., Bauer, R.M., Bizon, J.L., Roberson, E.D., and Ryan, L. (2018). Shared Functions of Perirhinal and Parahippocampal Cortices: Implications for Cognitive Aging. Trends Neurosci. *41*, 349–359.

Burwell, R.D. (2001). Borders and cytoarchitecture of the perirhinal and postrhinal cortices in the rat. J. Comp. Neurol. *437*, 17–41.

Burwell, R.D., and Hafeman, D.M. (2003). Positional firing properties of postrhinal cortex neurons. Neuroscience *119*, 577–588.

Chadwick, M.J., Jolly, A.E., Amos, D.P., Hassabis, D., and Spiers, H.J. (2015). A goal direction signal in the human entorhinal/subicular region. Curr. Biol. *25*, 87–92.

Chanales, A.J.H., Oza, A., Favila, S.E., and Kuhl, B.A. (2017). Overlap among Spatial Memories Triggers Repulsion of Hippocampal Representations. Curr. Biol. *27*, 2307–2317.e5.

Chen, X., Vieweg, P., and Wolbers, T. (2019). Computing distance information from landmarks and self-motion cues - differential contributions of anterior-lateral vs. posterior-medial entorhinal cortex in humans. Neuroimage *202*, 116074.

Clewett, D., DuBrow, S., and Davachi, L. (2019). Transcending time in the brain: how event memories are constructed from experience. Hippocampus *29*, 162–183.

Cohen, N., Pell, L., Edelson, M.G., Ben-Yakov, A., Pine, A., and Dudai, Y. (2015). Peri-encoding predictors of memory encoding and consolidation. Neurosci. Biobehav. Rev. *50*, 128–142.

Cole, M.W., Bassett, D.S., Power, J.D., Braver, T.S., and Petersen, S.E. (2014). Intrinsic and task-evoked network architectures of the human brain. Neuron *83*, 238–251.

Connor, C.E., and Knierim, J.J. (2017). Integration of objects and space in perception and memory. Nat. Neurosci. *20*, 1493–1503.

Copara, M.S., Hassan, A.S., Kyle, C.T., Libby, L.A., Ranganath, C., and Ekstrom, A.D. (2014). Complementary roles of human hippocampal subregions during retrieval of spatiotemporal context. J. Neurosci. *34*, 6834–6842.

Deuker, L., Bellmund, J.L.S., Navarro Schröder, T., and Doeller, C.F. (2016). An event map of memory space in the hippocampus. eLife *5*, e16534.

Doan, T.P., Lagartos-Donate, M.J., Nilssen, E.S., Ohara, S., and Witter, M.P. (2019). Convergent Projections from Perirhinal and Postrhinal Cortices Suggest a Multisensory Nature of Lateral, but Not Medial, Entorhinal Cortex. Cell Rep. *29*, 617–627.e7.

Doeller, C.F., King, J.A., and Burgess, N. (2008). Parallel striatal and hippocampal systems for landmarks and boundaries in spatial memory. Proc. Natl. Acad. Sci. USA *105*, 5915–5920.

Ekstrom, A.D. (2015). Why vision is important to how we navigate. Hippocampus *25*, 731–735.

Ekstrom, A.D., Arnold, A.E., and Iaria, G. (2014). A critical review of the allocentric spatial representation and its neural underpinnings: toward a network-based perspective. Front. Hum. Neurosci. *8*, 803.

Ekstrom, A.D., Huffman, D.J., and Starrett, M. (2017). Interacting networks of brain regions underlie human spatial navigation: a review and novel synthesis of the literature. J. Neurophysiol. *118*, 3328–3344.

Epstein, R.A. (2008). Parahippocampal and retrosplenial contributions to human spatial navigation. Trends Cogn. Sci. *12*, 388–396.

Epstein, R.A., Patai, E.Z., Julian, J.B., and Spiers, H.J. (2017). The cognitive map in humans: spatial navigation and beyond. Nat. Neurosci. *20*, 1504–1513.

Esteban, O., Markiewicz, C.J., Blair, R.W., Moodie, C.A., Isik, A.I., Erramuzpe, A., Kent, J.D., Goncalves, M., DuPre, E., Snyder, M., et al. (2019). fMRIPrep: a robust preprocessing pipeline for functional MRI. Nat. Methods *16*, 111–116.

Evensmoen, H.R., Ladstein, J., Hansen, T.I., Møller, J.A., Witter, M.P., Nadel, L., and Håberg, A.K. (2015). From details to large scale: the representation of environmental positions follows a granularity gradient along the human hippocampal and entorhinal anterior-posterior axis. Hippocampus *25*, 119–135.

Favila, S.E., Chanales, A.J.H., and Kuhl, B.A. (2016). Experience-dependent hippocampal pattern differentiation prevents interference during subsequent learning. Nat. Commun. *7*, 11066.

Frankó, E., Insausti, A.M., Artacho-Pérula, E., Insausti, R., and Chavoix, C. (2014). Identification of the human medial temporal lobe regions on magnetic resonance images. Hum. Brain Mapp. *35*, 248–256.

Furuya, Y., Matsumoto, J., Hori, E., Boas, C.V., Tran, A.H., Shimada, Y., Ono, T., and Nishijo, H. (2014). Place-related neuronal activity in the monkey parahippocampal gyrus and hippocampal formation during virtual navigation. Hippocampus *24*, 113–130.

Geerligs, L., Cam-Can, and Henson, R.N. (2016). Functional connectivity and structural covariance between regions of interest can be measured more accurately using multivariate distance correlation. Neuroimage *135*, 16–31.

Geib, B.R., Stanley, M.L., Wing, E.A., Laurienti, P.J., and Cabeza, R. (2017). Hippocampal Contributions to the Large-Scale Episodic Memory Network Predict Vivid Visual Memories. Cereb. Cortex *27*, 680–693.

Hansen, T.I., Haferstrom, E.C.D., Brunner, J.F., Lehn, H., and Håberg, A.K. (2015). Initial validation of a web-based self-administered neuropsychological test battery for older adults and seniors. J. Clin. Exp. Neuropsychol. *37*, 581–594.

Hirshhorn, M., Grady, C., Rosenbaum, R.S., Winocur, G., and Moscovitch, M. (2012). Brain regions involved in the retrieval of spatial and episodic details associated with a familiar environment: an fMRI study. Neuropsychologia *50*, 3094–3106.

Holland, D., Kuperman, J.M., and Dale, A.M. (2010). Efficient correction of inhomogeneous static magnetic field-induced distortion in Echo Planar Imaging. Neuroimage *50*, 175–183.

Horecka, K.M., Dulas, M.R., Schwarb, H., Lucas, H.D., Duff, M., and Cohen, N.J. (2018). Reconstructing relational information. Hippocampus *28*, 164–177.

Huffman, D.J., and Ekstrom, A.D. (2019). A Modality-Independent Network Underlies the Retrieval of Large-Scale Spatial Environments in the Human Brain. Neuron *104*, 611–622.e7.

Jacobs, J., Kahana, M.J., Ekstrom, A.D., Mollison, M.V., and Fried, I. (2010). A sense of direction in human entorhinal cortex. Proc. Natl. Acad. Sci. USA *107*, 6487–6492.

Jenkins, L.J., and Ranganath, C. (2016). Distinct neural mechanisms for remembering when an event occurred. Hippocampus *26*, 554–559.

Jeub, L.G.S., Sporns, O., and Fortunato, S. (2018). Multiresolution Consensus Clustering in Networks. Sci. Rep. *8*, 3259.

Kaas, J.H. (2005). From mice to men: the evolution of the large, complex human brain. J. Biosci. *30*, 155–165.

Kabsch, W. (1976). A solution for the best rotation to relate two sets of vectors. Acta Crystallogr. A *32*, 922–923.

Kim, M., and Maguire, E.A. (2018). Hippocampus, Retrosplenial and Parahippocampal Cortices Encode Multicompartment 3D Space in a Hierarchical Manner. Cereb. Cortex *28*, 1898–1909.

King, D.R., de Chastelaine, M., Elward, R.L., Wang, T.H., and Rugg, M.D. (2015). Recollection-related increases in functional connectivity predict individual differences in memory accuracy. J. Neurosci. *35*, 1763–1772.

Kolarik, B.S., Shahlaie, K., Hassan, A., Borders, A.A., Kaufman, K.C., Gurkoff, G., Yonelinas, A.P., and Ekstrom, A.D. (2016). Impairments in precision, rather than spatial strategy, characterize performance on the virtual Morris Water Maze: a case study. Neuropsychologia *80*, 90–101.

Kolarik, B.S., Baer, T., Shahlaie, K., Yonelinas, A.P., and Ekstrom, A.D. (2018). Close but no cigar: spatial precision deficits following medial temporal lobe lesions provide novel insight into theoretical models of navigation and memory. Hippocampus *28*, 31–41.

Koolschijn, R.S., Emir, U.E., Pantelides, A.C., Nili, H., Behrens, T.E.J., and Barron, H.C. (2019). The Hippocampus and Neocortical Inhibitory Engrams Protect against Memory Interference. Neuron *101*, 528–541.e6.

Kragel, P.A., Reddan, M.C., LaBar, K.S., and Wager, T.D. (2019). Emotion schemas are embedded in the human visual system. Sci. Adv. *5*, eaaw4358.

Kriegeskorte, N., and Bandettini, P. (2007). Analyzing for information, not activation, to exploit high-resolution fMRI. Neuroimage *38*, 649–662.

Kriegeskorte, N., Goebel, R., and Bandettini, P. (2006). Information-based functional brain mapping. Proc. Natl. Acad. Sci. USA *103*, 3863–3868.

Kyle, C.T., Stokes, J.D., Lieberman, J.S., Hassan, A.S., and Ekstrom, A.D. (2015). Successful retrieval of competing spatial environments in humans involves hippocampal pattern separation mechanisms. eLife *4*, e10499.

LaBar, K.S., and Cabeza, R. (2006). Cognitive neuroscience of emotional memory. Nat. Rev. Neurosci. *7*, 54–64.

Ladstein, J., Evensmoen, H.R., Håberg, A.K., Kristoffersen, A., and Goa, P.E. (2016). Effect of task-correlated physiological fluctuations and motion in 2D and 3D echo-planar imaging in a higher cognitive level fMRI paradigm. Front. Neurosci. *10*, 225.

LaRocque, K.F., Smith, M.E., Carr, V.A., Witthoft, N., Grill-Spector, K., and Wagner, A.D. (2013). Global similarity and pattern separation in the human medial temporal lobe predict subsequent memory. J. Neurosci. *33*, 5466–5474.

Miller, J.F., Neufang, M., Solway, A., Brandt, A., Trippel, M., Mader, I., Hefft, S., Merkow, M., Polyn, S.M., Jacobs, J., et al. (2013). Neural activity in human hippocampal formation reveals the spatial context of retrieved memories. Science *342*, 1111–1114.

Morgan, L.K., Macevoy, S.P., Aguirre, G.K., and Epstein, R.A. (2011). Distances between real-world locations are represented in the human hippocampus. J. Neurosci. *31*, 1238–1245.

Nau, M., Navarro Schröder, T., Frey, M., and Doeller, C.F. (2020). Behavior-dependent directional tuning in the human visual-navigation network. Nat. Commun. *11*, 3247.

Nichols, T., and Hayasaka, S. (2003). Controlling the familywise error rate in functional neuroimaging: a comparative review. Stat. Methods Med. Res. *12*, 419–446.

Nielson, D.M., Smith, T.A., Sreekumar, V., Dennis, S., and Sederberg, P.B. (2015). Human hippocampus represents space and time during retrieval of real-world memories. Proc. Natl. Acad. Sci. USA *112*, 11078–11083.

Nili, H., Wingfield, C., Walther, A., Su, L., Marslen-Wilson, W., and Kriegeskorte, N. (2014). A toolbox for representational similarity analysis. PLoS Comput. Biol. *10*, e1003553.

O'Keefe, J., and Burgess, N. (1996). Geometric determinants of the place fields of hippocampal neurons. Nature *381*, 425–428.

O'Keefe, J., and Conway, D.H. (1978). Hippocampal place units in the freely moving rat: why they fire where they fire. Exp. Brain Res. *31*, 573–590.

Penny, W.D., Friston, K.J., Ashburner, J.T., Kiebel, S.J., and Nichols, T.E. (2011). Statistical Parametric Mapping: The Analysis of Functional Brain Images (Elsevier).

Ramos, J.M.J. (2017). Perirhinal cortex involvement in allocentric spatial learning in the rat: Evidence from doubly marked tasks. Hippocampus *27*, 507–517.

R Development Core Team (2016). R: a language and environment for statistical computing (R Foundation for Statistical Computing).

Ritchey, M., Yonelinas, A.P., and Ranganath, C. (2014). Functional connectivity relationships predict similarities in task activation and pattern information during associative memory encoding. J. Cogn. Neurosci. *26*, 1085–1099.

Ritchey, M., Libby, L.A., and Ranganath, C. (2015). Cortico-hippocampal systems involved in memory and cognition: the PMAT framework. In Progress in Brain Research, S. O'Mara and M. Tsanov, eds. (Elsevier), pp. 45–64.

Robin, X., Turck, N., Hainard, A., Tiberti, N., Lisacek, F., Sanchez, J.-C., and Müller, M. (2011). pROC: an open-source package for R and S+ to analyze and compare ROC curves. BMC Bioinformatics *12*, 77.

Rolls, E.T., and Wirth, S. (2018). Spatial representations in the primate hippocampus, and their functions in memory and navigation. Prog. Neurobiol. *171*, 90–113.

Rosenke, M., Weiner, K.S., Barnett, M.A., Zilles, K., Amunts, K., Goebel, R., and Grill-Spector, K. (2018). A cross-validated cytoarchitectonic atlas of the human ventral visual stream. Neuroimage *170*, 257–270.

Rubinov, M., and Sporns, O. (2010). Complex network measures of brain connectivity: uses and interpretations. Neuroimage *52*, 1059–1069.

Saggar, M., Sporns, O., Gonzalez-Castillo, J., Bandettini, P.A., Carlsson, G., Glover, G., and Reiss, A.L. (2018). Towards a new approach to reveal dynamical organization of the brain using topological data analysis. Nat. Commun. *9*, 1399.

Schedlbauer, A.M., and Ekstrom, A.D. (2019). Flexible network community organization during the encoding and retrieval of spatiotemporal episodic memories. Netw. Neurosci. *3*, 1070–1093.

Schedlbauer, A.M., Copara, M.S., Watrous, A.J., and Ekstrom, A.D. (2014). Multiple interacting brain areas underlie successful spatiotemporal memory retrieval in humans. Sci. Rep. *4*, 6431.

Shine, J.P., Valdés-Herrera, J.P., Tempelmann, C., and Wolbers, T. (2019). Evidence for allocentric boundary and goal direction information in the human entorhinal cortex and subiculum. Nat. Commun. *10*, 4004.

Spiers, H.J., Burgess, N., Maguire, E.A., Baxendale, S.A., Hartley, T., Thompson, P.J., and O'Keefe, J. (2001). Unilateral temporal lobectomy patients show lateralized topographical and episodic memory deficits in a virtual town. Brain *124*, 2476–2489.

Stokes, J., Kyle, C., and Ekstrom, A.D. (2015). Complementary roles of human hippocampal subfields in differentiation and integration of spatial context. J. Cogn. Neurosci. *27*, 546–559.

Tolman, E.C. (1948). Cognitive maps in rats and men. Psychol. Rev. *55*, 189–208.

Traud, A.L., Kelsic, E.D., Mucha, P.J., and Porter, M.A. (2011). Comparing Community Structure to Characteristics in Online Collegiate Social Networks. SIAM Rev. *53*, 526–543.

Tversky, B. (1992). Distortions in cognitive maps. Geoforum *23*, 131–138.

Umeyama, S. (1991). Least-squares estimation of transformation parameters between two point patterns. IEEE Trans. Pattern Anal. Mach. Intell. *13*, 376–380.

van den Heuvel, M.P., and Sporns, O. (2013). Network hubs in the human brain. Trends Cogn. Sci. *17*, 683–696.

Wager, T.D., and Nichols, T.E. (2003). Optimization of experimental design in fMRI: a general framework using a genetic algorithm. Neuroimage *18*, 293–309.

Wahlstrom, K.L., Huff, M.L., Emmons, E.B., Freeman, J.H., Narayanan, N.S., McIntyre, C.K., and LaLumiere, R.T. (2018). Basolateral Amygdala Inputs to the Medial Entorhinal Cortex Selectively Modulate the Consolidation of Spatial and Contextual Learning. J. Neurosci. *38*, 2698–2712.

Walther, A., Nili, H., Ejaz, N., Alink, A., Kriegeskorte, N., and Diedrichsen, J. (2016). Reliability of dissimilarity measures for multi-voxel pattern analysis. Neuroimage *137*, 188–200.

Warren, W.H., Rothman, D.B., Schnapp, B.H., and Ericson, J.D. (2017). Wormholes in virtual space: from cognitive maps to cognitive graphs. Cognition *166*, 152–163.

Weiner, K.S., and Zilles, K. (2016). The anatomical and functional specialization of the fusiform gyrus. Neuropsychologia *83*, 48–62.

Westphal, A.J., Wang, S., and Rissman, J. (2017). Episodic Memory Retrieval Benefits from a Less Modular Brain Network Organization. J. Neurosci. *37*, 3523–3531.

Winkler, A.M., Ridgway, G.R., Webster, M.A., Smith, S.M., and Nichols, T.E. (2014). Permutation inference for the general linear model. Neuroimage *92*, 381–397.

Wolbers, T., and Wiener, J.M. (2014). Challenges for identifying the neural mechanisms that support spatial navigation: the impact of spatial scale. Front. Hum. Neurosci. *8*, 571.

Xia, M., Wang, J., and He, Y. (2013). BrainNet Viewer: a network visualization tool for human brain connectomics. PLoS ONE *8*, e68910.

Zhang, H., and Ekstrom, A. (2013). Human neural systems underlying rigid and flexible forms of allocentric spatial representation. Hum. Brain Mapp. *34*, 1070–1087.

STAR★METHODS

KEY RESOURCES TABLE

REAGENT or RESOURCE	SOURCE	IDENTIFIER
Software and algorithms		
fMRI paradigm	Property of NTNU (fMRI group)	
fMRIprep	(Esteban et al., 2019)	https://fmriprep.readthedocs.io/en/stable/index.html; RRID:SCR_016216
MATLAB R2018a	Mathworks	https://www.mathworks.com; RRID:SCR_001622
SPM 12	(Penny et al., 2011)	https://www.fil.ion.ucl.ac.uk/spm/software/; RRID:SCR_007037
RSA toolbox	(Nili et al., 2014)	https://git.fmrib.ox.ac.uk/hnili/rsa; RRID:SCR_019029
FSL 5.0.9	Analysis Group, FMRIB, Oxford, UK	https://fsl.fmrib.ox.ac.uk/fsl/fslwiki; RRID:SCR_002823
Brain Connectivity toolbox	(Rubinov and Sporns, 2010)	https://sites.google.com/site/bctnet/; RRID:SCR_004841
Z-score of the Rand coefficient	(Traud et al., 2011)	http://commdetect.weebly.com/#
BrainNet Viewer	(Xia et al., 2013)	https://www.nitrc.org/projects/bnv/; RRID:SCR_009446
R 3.6.3	R Foundation for Statistical Computing	https://www.R-project.org/; RRID:SCR_001905
R-package pROC	(Robin et al., 2011)	https://cran.r-project.org/web/packages/pROC/index.html
R-package lme4	(Bates et al., 2015)	https://cran.r-project.org/web/packages/lme4/index.html
R-package sjPlot	R Foundation for Statistical Computing	https://cran.r-project.org/web/packages/sjPlot/index.html
R-package AICcmodavg	R Foundation for Statistical Computing	https://cran.r-project.org/web/packages/AICcmodavg/index.html

RESOURCE AVAILABILITY

Lead contact

Further information and requests for resources and reagents should be directed to and will be fulfilled by the Lead Contact, Hallvard Røe Evensmoen (hjernemannen@gmail.com).

Materials availability

This study neither used any reagent nor generated new materials

Data and code availability

Access to data by qualified investigators are subject to scientific and ethical review and must comply with the European Union General Data Protection Regulations (GDPR), Norwegian laws and regulations, and NTNU regulations. Completion of a material transfer agreement (MTA) signed by an institutional official will be required in order to access the data. Access to the fMRI paradigm can be achieved through completion of a material transfer agreement (MTA) signed by an institutional official.

EXPERIMENTAL MODEL AND SUBJECT DETAILS

Participants

Thirty-one men (18 - 27 years, mean 21 years) with no history of neurological disorders, head trauma, previous or current DSM-IV axis I diagnosis of psychiatric illness, including substance abuse, were recruited. Moreover, we only recruited male subjects in order to reduce variability in the data. They were all right handed, ascertained with the Edinburgh Handedness Inventory, with mean score 88.4 ± 29.7%. All participants provided written informed consent prior to participation and received 1000 Norwegian kroner as reimbursement. The study was approved by the Regional Committee for Medical Research Ethics in central Norway.

METHOD DETAILS

Image acquisition

Functional and anatomical MR images were acquired with a 32-channel Head Matrix Coil on a 3T Siemens Trio scanner, and on a 3T Siemens Skyra scanner replacing the Trio for the last seven participants (Siemens AG, Erlangen, Germany) (see Ladstein et al., 2016). Foam pads were used to minimize head motion. The fMRI stimuli were presented using a LCD monitor with 1280 × 1024 resolution, and the subject moved inside the environment using a MRI compatible joystick (Current Designs, Philadelphia, US). The participants were first allowed to familiarize themselves with the presentation equipment and joystick, and then completed practice trials from the different experimental conditions. Scanning was commenced when complete task compliance was ensured.

T2* weighted, blood-oxygen-level-dependent (BOLD) sensitive images were acquired during the environmental encoding task, using a 2D echo-planar imaging pulse sequence and limited field of view (FOV) optimized to cover the medial temporal lobe with highest possible spatial resolution. The slices were positioned as close to 90° on the anterior-posterior direction of the hippocampus as possible. FOV = 220 mm x 220 mm, slice thickness = 1.9 mm (no gap), number of slices = 40, matrix = 116x116 yielding 1.9x1.9x1.9mm^3 voxels (TR = 2110.8 ms, TE = 28 ms, flip angle = 90°). For the last seven participants, the 2D echo-planar imaging parameters differed slightly (FOV = 220 mm x 220 mm, slice thickness = 2.0 mm (no gap), number of slices = 40, matrix = 116x116 yielding 1.9x1.9x2.0mm^3 voxels, TR = 2253.2 ms, TE = 28 ms, flip angle = 90°). GRAPPA acceleration was used, with a factor of four. Scanning parameters were optimized for reduction of susceptibility-induced signal loss in areas near the medial temporal lobe, and there was no effect of an anterior-posterior distortion correction (Holland et al., 2010), so this step was dropped from the image preprocessing. Each functional run contained 143 volumes, and for the last seven participants 134 volumes. For anatomical reference, a T1 weighted (T1W) 3D volume was acquired using a MPRAGE sequence (TR = 2300 ms, TE = 2.94 ms, FOV = 256 mm x 256 mm x 192 mm, matrix 256x256x192 yielding a resolution of 1.0x1.0x1.0 mm^3, flip angle = 8°).

fMRI paradigm

The participants were exposed to a total of 35 virtual environments during BOLD fMRI scanning. The fMRI paradigm was a block design consisting of seven runs, with 5 blocks in each run, with one environment per block. Within each block, there were three periods; environmental exploration (30 s), post-exploration (with fixation cross; 15 s), and an odd-even task (15 s) (Figure 1A). Between runs, the participants were tested on recall of environmental information from each of the five blocks. The environments were presented in a random sequence across participants, within and between runs.

Each environment was a room with a door and an outer perimeter (walls), which had one of 10 geometric shapes. All environments were between 50 and 90 virtual m^2 large and contained five unique, unrelated objects (Figures 1A and 1B). Within each environment, the objects were positioned in a unique pattern (Figure 1B). In the environmental exploration period, the participants started out positioned at the door of the room (environment) and were free to explore the environment from a first-person perspective (using a joystick with moving speed set to two virtual m/s) (Figure 1A). Average movement across all participants and all environments was 26.4 ± 7.8 virtual meters. The participants were instructed to memorize the environment in the post-exploration period, while fixating on a cross on the computer screen. During the odd-even task, the participants were instructed to push the right joystick button when an even number (< 100) appeared on the screen and the left joystick button when an odd number (< 100) appeared (numbers presented at random). The participants were explicitly instructed to focus on getting the odd-even judgments correct, and behavioral data were analyzed to verify compliance. The purpose of the odd- even period was to function as an implicit baseline for fMRI data analysis.

The virtual environments were developed in collaboration with Terra Vision AS (Terra Vision, Trondheim, Norway) using the Torque game engine (Garage Games, Eugene, Oregon, US).

Tests between the runs

Between runs, with no ongoing functional image acquisition, the participants were given three sets of tests (1-3) that assessed recall of various spatial and non-spatial information from each of the five recently learned environments (Figures 1B and 1C). The participants viewed the tests on the computer screen while lying in the scanner and responded by dragging and dropping objects using the joystick. The tests were programmed using HTML and JavaScript (Hansen et al., 2015). Data from the first two tests were not used in the analyses presented in this paper. The first test (1) assessed recall of which objects had been presented together, i.e., in the same environment. In the second test (2), the participants were asked to assign a given group of objects to the environment in which they had been presented, based on the geometry of the perimeter of the environment. Finally (3), the participants performed the allocentric position test (Figure 1b), from which several allocentric measures were obtained (detailed below; see Figure 1C). For each environment (block), the five objects belonging to that environment were presented next to a 2D overview of the environment (see Figure 1B), and the participants were asked to drag and drop each object into its original location. Participants were instructed to position each object as accurately as possible. Three allocentric measures were derived: Pattern accuracy, Environmental geometry, and Euclidean map (Figure 1C); Object identity was also assessed (see explanation below).

Measures of post-exploration accuracy

Pattern accuracy indicates whether the participant accurately reproduced the positional pattern of the five objects presented in a given block, regardless of the identity of the objects (Figure 1C). The participant response (drag-and-drop into the 2D overview)

was translated so that the geometric center (centroid) of the recalled positional pattern matched the center of the correct positional pattern (as originally presented during the environmental exploration period). Then the recalled positional pattern was rotated into alignment with the correct positional pattern, minimizing the root mean square deviation between the patterns (Kabsch, 1976). Next, the recalled positional pattern was scaled (up or down) minimizing the root mean square deviation between the patterns (Umeyama, 1991). The purpose of the first two transformations (translation, rotation) was to disentangle the positional pattern as such from its relation to the environment's perimeter (walls of the room). The purpose of scaling was to account for the fact that human spatial representations are sometimes compressed or expanded (Tversky, 1992). After these transformations, Pattern accuracy was obtained as the inverse of the total sum of squares error after all transformations had been performed. That is, for each position in the transformed positional pattern, the squared error was obtained with respect to the closest position in the correct positional pattern, and all such squared errors were summed to obtain a total sum of squares error. Pattern accuracy was classified as fine, medium, coarse, or ''failed.'' The thresholds between coarse, medium, and fine were defined such that, across participants, the number of trials in each category was identical (after chance level was determined; see below). Responses were categorized as ''failed'' if the level of accuracy did not exceed chance level (see below).

Environmental geometry indicates how accurately the recalled positional pattern was located relative to the perimeter of the environment (Figure 1C). It was defined as the difference between Pattern accuracy and the inverse of the total sums of squares for the recalled positional pattern before translation, rotation, and scaling. Thus, high Environmental geometry implies a low degree of rotation, translation, and scaling relative to the perimeter of the environment. Responses were classified as fine, medium, coarse, or ''failed,'' as described above.

The third allocentric measure obtained from the allocentric position test was Euclidean map, defined as a response obtaining high scores on both Pattern accuracy and Environmental geometry (Figure 1C). A high Euclidean map score means the participant correctly recalled the positional pattern as such, i.e., the angles and relative distances between the objects, as well as accurately recalling the positioning of this pattern relative to the perimeter of the environment.

Finally, Object identity indicates how accurately the participant recalled which object was placed where within the positional pattern (Figure 1C) (requiring at least a ''coarse'' level of Pattern accuracy; if Pattern accuracy was ''failed,'' Object identity was not calculated). Participant responses were classified into three categories according to number of objects correctly remembered: 0-1, 2, 3-5 (see below).

Post-experiment questionnaire

After MRI scanning, the participants were given a questionnaire designed to find out which strategies the participants had employed in order to successfully encode environmental features. The questionnaire had a nine-point scale, ranging from ''strongly agree'' (9) to ''strongly disagree'' (1). The participants indicated to what extent they agreed with the following statements: (a) ''I knew the positions of the objects from a first person perspective after the environmental exploration period''; (b) ''I knew the relative positions of the objects from a 3rd person perspective after the environmental exploration period''; (c) ''I associated the objects together into a coherent representation during the environmental exploration period''; (d) ''In the post-exploration period, I imagined the environment from a first person perspective''; (e) ''In the post-exploration period, I imagined the environment from a bird's eye view''; and (f) ''In the post-exploration period, I envisioned the environment as a whole.'' The post-experiment questionnaire revealed that the participants visualized the environments from both a first-person perspective (on a scale from 1 to 9, the average score was 7.3 ± 1.7 for the environmental exploration period and 6.8 ± 2.5 for the post-exploration period) and a third-person perspective (environmental exploration period: 6.8 ± 2.3; post-exploration period: 5.0 ± 3.1) (Evensmoen et al., 2015).

fMRI preprocessing

Preprocessing of the fMRI data was performed using FMRIPREP (Esteban et al., 2019) (https://fmriprep.readthedocs.io/en/stable/index.html), a Nipype based tool (https://nipype.readthedocs.io/en/latest/). Each T1-weighted volume was corrected for intensity non-uniformity using N4BiasFieldCorrection v2.1.0 and skull-stripped using antsBrainExtraction.sh v2.1.0 (using the OASIS template) (ANTs v2.1.0, http://stnava.github.io/ANTs/). Brain surfaces were reconstructed using recon-all from FreeSurfer v6.0.0 (https://surfer.nmr.mgh.harvard.edu/fswiki), and the brain mask estimated previously was refined with a custom variation of the method to reconcile ANTs-derived and FreeSurfer-derived segmentations of the cortical gray-matter of Mindboggle (https://mindboggle.info/). Spatial normalization to the ICBM 152 Nonlinear Asymmetrical template version 2009c (http://www.bic.mni.mcgill.ca/ServicesAtlases/ICBM152NLin2009) was performed through nonlinear registration with the *antsRegistration* tool of ANTs, using brain-extracted versions of both T1-weighted volume and template. Brain tissue segmentation of cerebrospinal fluid, white-matter, and gray-matter was performed on the brain-extracted T1-weighted image using fast (FSL v5.0.9). Functional data were motion corrected using *mcflirt* (FSL). This was followed by co-registration to the corresponding T1-weighted image using boundary-based registration with 9 degrees of freedom, using bbregister (FreeSurfer v6.0.0). Motion correcting transformations, BOLD-to-T1w transformation and T1w-to-template (MNI) warp were concatenated and applied in a single step using *antsApplyTransforms* with Lanczos interpolation.

Regions of interest

An MTL mask was used in all fMRI analyses. This mask included all subregions within the MTL bilaterally (Frankó et al., 2014), as well as MTL white matter. To make sure that the parahippocampal place area was covered, the lingual gyrus and the fusiform gyrus were

also included (Epstein, 2008). The entorhinal and perirhinal cortices were divided into an anterior subregion and a posterior subregion based on finding the central MNI-coordinate along the anterior-posterior axis, and similarly into a lateral subregion and a medial subregion based on finding the central MNI-coordinates along the lateral/medial axis for each MRI slice.

QUANTIFICATION AND STATISTICAL ANALYSIS

Behavioral data analysis

The purpose of including a category of "failed" responses was to be able to identify trials where it was unlikely that allocentric encoding had taken place, such that including these trials would introduce noise into the analyses. "Failed" was defined as "accuracy (Pattern, Environmental geometry, Euclidean map, or Object identity) at or below chance level." Chance level was estimated by comparing the distribution of scores when a recalled positional pattern was compared to the correct positional pattern, with the distribution of scores when the response was compared to the correct positional patterns from an extended set of 120 environments (excluding the correct one) (Figure S1A). The optimal cut-off value between these two distributions was estimated using R 3.3.3 (R Development Core Team, 2016) and the pROC package (Robin et al., 2011). We constructed a receiver operating characteristics (ROC) curve by plotting true positive fraction (sensitivity) versus true negative fraction (specificity) for different thresholds (or cut-off values) between the two distributions (Figure S1B). The optimal threshold between the two distributions was estimated by minimizing the misclassification fractions, using the best method argument in the pROC package. For Pattern accuracy and Environmental geometry, the thresholds between fine, medium, and coarse trials were defined so that the average number of trials in each category was identical, using three significant digits, across participants. For Pattern accuracy, the thresholds were 3919 and 9335, and for Environmental geometry 6290 and 14775. For Euclidean map, the average number of trials was 5.6 ± 4.5 for fine, 10.6 ± 4.0 for medium, and 14.0 ± 4.0 for coarse. Finally, the two-sided Wilcoxon signed rank test was used to assess whether the average Pattern accuracy score was higher for fine Euclidean map than fine Pattern accuracy and whether the average Environmental boundary accuracy score was higher for fine Euclidean map than fine Environmental boundary. A significance level of alpha = 0.05 was used corrected for multiple comparisons using a 5% false discovery rate (FDR).

When measuring accurate recall of Object identity, only trials where Pattern accuracy was above chance level were included. The object position score was divided into correct recall of the positions of three or more objects (3-5 obj) (avg. no. of environments: 2.8 ± 1.7), two objects (2 obj) (avg. no. of environments: 10.1 ± 4.1), and one or no object (0-1 obj) (avg. no. of environments: 18.6 ± 2.5).

Activation pattern similarity analyses

The fMRI data were first subjected to a univariate (single-subject) analysis in SPM 12 (Penny et al., 2011). Brain activity was modeled using a general linear model (GLM) with the default options. Three models were used to investigate associations between accuracy measurements and activation pattern dissimilarity. The first model was used to investigate Pattern accuracy, the second Environmental geometry and Euclidean map, and the third, object identity. In the first model, the independent variables were, in addition to intercept, Pattern accuracy (with four levels: fine, medium, coarse, and failed) for the environmental exploration period and for the post-exploration period, resulting in a total of 9 regressors (see Figure S2A). The odd-even condition served as implicit baseline. In the second model, only regressors for trials with at least a "coarse" score on Pattern accuracy were included. Therefore, two extra covariates were added, one representing failed Pattern accuracy for the exploration period and one for the post-exploration period; hence, the total number of regressors for Environmental geometry and Euclidean map was 11. In the third model, the levels of accuracy for Object identity were 0-1 (coarse), 2 (medium), and 3-5 (fine); here there was no "failed" condition, and only regressors for trials with at least "coarse" on Pattern accuracy were included), resulting in a total of 9 regressors for Object identity. These models allow the BOLD response in a given voxel to be non-linearly modulated by level of accuracy. One participant was excluded from the Pattern accuracy analysis, four from the Euclidean map analysis, and three from the Object identity analysis, due to lack of trials in one level of encoding.

In order to test for associations between encoding accuracy and changes in MTL activation patterns, we used a multivariate representational similarity analysis (RSA) (Nili et al., 2014), implemented in MATLAB (R2018a, Mathworks, Natick, Massachusetts, U.S.A.). The multivariate analysis was restricted to the MTL mask described above. A spherical "searchlight" was obtained for each voxel using a maximum radius of 10 mm to create searchlights consisting of 30 voxels (each 2 mm^3). This resulted in an average searchlight radius of 4 mm, previously shown to be optimal for detection performance (Kriegeskorte et al., 2006). Non-spherical searchlights were allowed for voxels close to the borders of the MTL to make sure that each searchlight contained the same number of voxels. The searchlights were investigated separately and independently of each other. For each searchlight, three activation maps were generated, containing the betas from the univariate GLM analysis for "fine," "medium," or "coarse"(0-1, 2, 3-5 for Object identity) with odd-even as an implicit baseline (see Figure S2A). A multivariate noise normalization was then applied to these activation maps, by first extracting the GLM residual for each voxel, then using those residuals to create a covariance matrix between all voxels, and finally using that covariance matrix to perform a spatial pre-whitening of the regression coefficients (Walther et al., 2016). The next step was to generate pairwise activation pattern dissimilarity maps for fine versus medium, fine versus coarse, and medium versus coarse, using an Euclidean distance measure (equivalent to computing the Mahalanobis distance between activity patterns) (Walther et al., 2016). Subsequently, in order to assess whether the activation pattern dissimilarity was consistently modulated across all levels of accuracy, the dissimilarity maps were correlated with a model representing an increasing order of dissimilarity from coarse through

medium to fine (Figures 2A and S2A). Thus, for the central voxel of the searchlight region a correlation score was obtained that expressed the degree to which the similarity of activation patterns centered around that voxel were consistently modulated by accuracy (coarse-medium-fine). Kendall's τ_A was used to assess whether the observed activation pattern dissimilarities could be predicted by the accuracy model, because it also allows monotonic (not strictly linear) relationships (Nili et al., 2014). Smoothing was performed on the single-subject level after estimation of the activation pattern dissimilarities, so as not to reduce the "spatial fine structure of the data" (Kriegeskorte et al., 2006), and the resulting correlation maps were smoothed with a Gaussian kernel of 4 mm. To test whether the correlation effects were significantly different from zero at group level, the smoothed correlation maps were tested non-parametrically with one-sample permutation based t tests using the program Randomise (Winkler et al., 2014), part of the FSL software package. In addition, to test if there was a relationship between the correlation effects and mean individual success rate, we ran the group level model with the average success rate across subjects as a covariate. Inference used cluster mass statistics (Bullmore et al., 1999; Nichols and Hayasaka, 2003), with a cluster forming threshold set at $p = 0.0005$. The cluster mass threshold takes into account both the size of the clusters and the activation effect of the voxels within the cluster (Bullmore et al., 1999). Clusters were considered significant at $p = 0.05$, corrected for multiple testing using the non-parametric distribution of the maximum statistic. For visualization purposes, the data were resampled to $1mm^3$ resolution.

The analysis procedure described in the previous paragraph evaluates whether activation pattern dissimilarity is consistently modulated by increasing level of accuracy. However, it does not determine whether activation pattern dissimilarity is driven by the most accurate ("fine") or the least accurate ("coarse") trials. In order to determine that, we obtained activation pattern dissimilarity estimates for fine versus baseline (last five seconds of odd-even) and for coarse versus baseline. In this analysis, the first approximately 10 s of the odd-even period functioned as implicit baseline, and the last 5 s of odd-even were added as a covariate for the purpose of comparison with "fine" and "coarse." First, as before, brain activity was modeled on the single-subject level in SPM 12, using a GLM with similar models as in the initial analyses, with the exception that the odd-even period now was split, as described above. Second, the data were taken into the RSA toolbox, and activation pattern dissimilarities were estimated for searchlights centered on voxels that showed a peak effect for encoding of allocentric accuracy or object id. Third, to get an overall estimate of whether activation pattern dissimilarity within the medial temporal lobe was driven by "fine" or "coarse" trials, we used mixed linear models with maximum likelihood estimates. The data were analyzed in R, using the mixed linear model package lme4 (Bates et al., 2015). The R package sjPlot was used for visualization. In these analyses, activation pattern dissimilarity was employed as the dependent variable, and independent variables were selected on the basis of whether their inclusion improved the second-order AIC (Akaike information criteria) value of the model (https://cran.r-project.org/web/packages/AICcmodavg/index.html). In addition, absolute measures of goodness-of-fit were evaluated to determine whether the included variables indeed were informative. First, we tested for random intercepts across participants. The fixed effects independent variables tested for inclusion in the model were encoding accuracy (accurate and least accurate), time (environmental exploration and post-exploration), and allocentric measure (Pattern accuracy, Environmental geometry, and Euclidean map). A similar analysis was then conducted for Object identity, using correct recall of the positions of three or more objects (3-5 obj) instead of "fine" and correct recall of one object or none (0-1 obj) instead of "coarse."

To confirm the validity of our RSA results we ran a leave-one-subject out crossvalidated nearest neighbor classifiers procedure in MATLAB, with the predicted dissimilarities in the model RDM (see Figure 2A) as classes. First, we extracted normalized activation pattern dissimilarity matrices for each peak voxel ROI from the Euclidean map, Pattern accuracy, Environmental geometry, and Object position RSA analysis. Second, a five-nearest neighbor classifier (with Euclidean distance as distance metric) was trained on the dissimilarity matrices for each of the functional ROIs and n-1 subjects, and then the classifier was tested on the left out subject. Third, chance level for the classification was estimated by shuffling a vector with the classes used in classification and comparing that against a vector with the correct classes 5000 times and estimating the average across all 5000 permutations. Finally, the two-sided Wilcoxon signed rank test was used to assess whether the classification accuracies were above chance level. A significance level of alpha = 0.05 was used, corrected for multiple comparisons using a 5% false discovery rate (FDR). The peak voxel ROIs used consisted of the peak voxel as well as neighboring voxels, resulting in seven voxels in total (to allow for some individual anatomical variation).

Representational connectivity

We assessed functional connectivity between the MTL structures that were involved in environmental encoding (see Figure 3). This connectivity analysis was limited to searchlights centered on voxels that showed a local peak effect for allocentric or object encoding (see above) (Figure 3A). These searchlights originated from four separate GLMs, i.e., Pattern accuracy, Environmental geometry, Euclidean map, and Object identity, thus avoiding the introduction of unwanted dependencies among the tests. Functional connectivity was defined as the extent to which these searchlights showed a similar change in activation pattern dissimilarity from one environment to another throughout the experiment, as assessed by a multivariate distance correlation (Basti et al., 2020; Geerligs et al., 2016; Ritchey et al., 2014; Stokes et al., 2015). First, the activity was modeled on a single-subject level in SPM 12, using a univariate GLM with, in addition to the intercept, one independent variable for each exploration and post-exploration period (see Figure 3A). This resulted in a total of 71 regressors. The Odd-even period was used as an implicit baseline in the univariate GLM. The data were then taken into the RSA toolbox, and an activation pattern dissimilarity matrix (RDM) was estimated for each searchlight. For the searchlights that showed peak effect for allocentric or object encoding during environmental exploration, the RDM was limited to activation

pattern dissimilarities between environmental exploration periods. Similarly, for searchlights that showed peak effect related to allocentric or object encoding during the post-exploration period, the RDM was limited to activation pattern dissimilarities between post-exploration periods. For each subject, pairwise correlation analyses (Kendall's τ_A) between the searchlight-specific RDMs (Nili et al., 2014) produced one correlation matrix for the environmental exploration periods and one for the post-exploration periods. A higher Kendall's τ_A was interpreted as indicating stronger functional connectivity. The two-sided Wilcoxon signed rank test was performed on a group level, allowing for assessment of whether the connectivity (Kendall's τ_A) between pairs of searchlights or nodes was significant. A significance level of alpha = 0.05 was used, corrected for multiple comparisons using a 5% false discovery rate (FDR).

Graph analysis

Graph analyses of the allocentric network were performed separately for the environmental exploration and the post-exploration period, consisting of (1) a multiresolution consensus clustering analysis to evaluate hierarchical connectivity (Jeub et al., 2018), (2) evaluation of the centrality of individual nodes within the network by using graph measures from the Brain Connectivity toolbox (Rubinov and Sporns, 2010) (https://sites.google.com/site/bctnet/), and (3) analysis of the relationship between average behavioral performance and global graph measures from the Brain Connectivity toolbox. The average network across all the participants was investigated. In addition, the participants' individual networks were analyzed to explore individual differences in connectivity. Negative edge weights were set to zero.

First, a multiresolution consensus clustering analysis (Jeub et al., 2018) was used to evaluate the level of hierarchical organization within the allocentric MTL network. We applied an event sampling procedure to estimate the modular partitioning of the network for a set of 10000 samples (see below) that covered all scales present in the network approximately equally. Modularity for each sample was evaluated using the iterated GenLouvain algorithm, resulting in a set of multiresolution partitions. The complete set of multiresolution partitions was then tested for hierarchical clustering using a divisive consensus clustering algorithm. The hierarchical consensus clustering algorithm started with the partition where all nodes were part of one module, and then divided all modules based on significant pairwise co-classification of nodes until no module could be further subdivided. This resulted in a tree of nested partitions, with a set of levels that each represented a unique partition. A test level of alpha < 0.05 was used for all branches in the tree (see below). The sample size and the p value threshold in the multiresolution clustering analysis were selected by evaluating which combination of p value threshold (0.05, 0.01,0.001, or 0.0001) and partition size in the initial ensemble (1000, 10000, 100000, or 1000000) that gave the highest average Z-score of the rand-coefficient, when comparing the finest-level partition for each combination of p value threshold and partition size with the finest-level partition for all other combinations of p value thresholds and number of partitions. Further, we extracted the number of modules in the top-level partition of the tree. Finally, to compare the top-level partition for each individual with the top-level partition estimated at a group level we used the adjusted Rand similarity coefficient and the Z-score of the Rand coefficient if the adjusted Rand similarity coefficient was relatively small (positive Z-scores imply that the partitions are similar) (Traud et al., 2011).

We also included "leave-one subject out" and "leave-one trial out" cluster stability analyses. The "leave-one subject out" analysis involved removing the data from one subject before running the multiresolution consensus clustering analysis, and then comparing the top-level partition from this analysis with the top-level partition from all the subjects (similar to the cluster stability analysis implemented in the R package clValid (Brock et al., 2008) (https://cran.r-project.org/web/packages/clValid/index.html)). The measure used for this comparison was the adjusted Rand similarity coefficient, and the Z-score of the Rand coefficient in cases where the adjusted Rand similarity coefficient was relatively small (Traud et al., 2011). The "leave-one trial out" was identical to the "leave-one subject out" except that individual trials were left out of the analysis instead of subjects.

Second, a set of measures that described the centrality of the nodes in the allocentric network and the overall global efficiency of the allocentric network were estimated using the Brain Connectivity toolbox (Rubinov and Sporns, 2010) in MATLAB. For the individual nodes within the network from each subject, degree centrality, betweenness centrality, eigenvector centrality, participation, within-module degree z-score, strength, and clustering were estimated. The scores for these individual node measures were then standardized within the subject-specific allocentric MTL networks:

$$z_i = \frac{x_i - \mu}{\sigma},\ 1 \leq i \leq N$$

using the mean μ and the standard deviation σ across all nodes. Finally, for each node in the allocentric MTL network a two-sided Wilcoxon signed rank test was performed on the group level for each of the centrality measures, to assess whether any of the nodes showed a higher level of centrality than the other nodes. A significance threshold of p = 0.05 was used, corrected for multiple comparisons using a 5% False Discovery Rate (FDR). The brain networks were visualized using the BrainNet Viewer (Xia et al., 2013). For the network as a whole, global efficiency was estimated (see (Bullmore and Sporns, 2012; Rubinov and Sporns, 2010) for details and interpretations of these measures).

Third, we explored the relationships between average behavioral performance (Pattern accuracy, Environmental geometry, Euclidean map, Object identity) and global graph measures from the participants' individual networks (global efficiency and number of top-level modules in the allocentric network). The global graph measures were used as dependent variables in separate mixed linear models implemented in R, as described above. The independent variables were selected on the basis of whether their inclusion improved the second-order AIC value in each case. First, we tested for random intercepts across participants. The fixed effects

independent variables tested for inclusion were all spatial measures in separate models (Pattern accuracy, Environmental geometry, Euclidean map, and Object identity), time (environmental exploration and post-exploration), interaction effects (''spatial measure'' * time), while the global graph measure density was included as a nuisance variable (see Table S7). Once the best model was selected, the relationship between behavioral performance and global graph measure was tested for statistical significance. A significance threshold of $p = 0.05$ was used, and the analyses were FDR corrected for the total number of explanatory variables, across all models, (Table S7), with a 5% expected false positive rate.

Temporal signal-to-noise ratio

Finally, we evaluated the temporal SNR (signal-to-noise ratio) (mean signal over time divided by the temporal standard deviation) for the searchlights that showed a peak effect (for the Euclidean map, Pattern accuracy, Environmental geometry, or Object position RSA analysis) using FSL. First, to evaluate if the temporal SNR differed across the searchlights, the different searchlights were used as a dependent variable and temporal SNR as an independent variable in mixed linear models implemented in R, as described above. Second, to evaluate if variability in SNR across the searchlights could explain the variability in the main graph measures used, degree centrality and participation were used as dependent variables and temporal SNR as an independent variable in mixed linear models. The Environmental exploration period and Post-exploration period were analyzed separately. The significance threshold was corrected for the total number of explanatory variables, across all models, using a 5% False Discovery Rate (FDR).